Advancing MɪNNLO_PS to diboson processes: $Z\gamma$ production at NNLO+PS

Daniele Lombardi, Marius Wiesemann and Giulia Zanderighi

Max-Planck-Institut für Physik,
Föhringer Ring 6, 80805 München, Germany

E-mail: lombardi@mpp.mpg.de, marius.wiesemann@cern.ch,
zanderi@mpp.mpg.de

ABSTRACT: We consider $Z\gamma$ production in hadronic collisions and present the first computation of next-to-next-to-leading order accurate predictions consistently matched to parton showers (NNLO+PS). Spin correlations, interferences and off-shell effects are included by calculating the full process $pp \to \ell^+\ell^-\gamma$. We extend the recently developed MɪNNLO_PS method to genuine $2 \to 2$ hard scattering processes at the LHC, which paves the way for NNLO+PS simulations of all diboson processes. This is the first $2 \to 2$ NNLO+PS calculation that does not require an a-posteriori multi-differential reweighting. We find that both NNLO corrections and matching to parton showers are crucial for an accurate simulation of the $Z\gamma$ process. Our predictions are in very good agreement with recent ATLAS data.

Contents

1 Introduction

Lacking clear hints for new-physics phenomena, particle phenomenology at the Large Hadron Collider (LHC) has entered the precision era. The accurate measurement of Standard Model (SM) processes provides a valuable alternative in the discovery of new physics through small deviations from SM predictions. Many LHC reactions, in particular colour-singlet processes, are not only measured, but also predicted at a remarkable accuracy. For instance the recent $Z\gamma$ [1] and ZZ [2] measurements include the full Run-2 data and are hitting percent-level uncertainties even for differential observables. The vast amount of data collected at the LHC will continuously decrease experimental uncertainties, thereby demanding accurate theory predictions in many relevant physics processes.

The theoretical description of fiducial cross sections and kinematic distributions has been greatly improved by the calculation of NNLO corrections in QCD perturbation theory. Those have become the standard for $2 \to 1$ and $2 \to 2$ colour-singlet processes [3–35] by now. The recent NNLO calculation of $\gamma\gamma\gamma$ production [36, 37] marks another milestone for precision calculations, since it is the first $2 \to 3$ LHC process to be computed at this level of precision. The comparison of theoretical predictions to LHC measurements highlights the fact that the knowledge of NNLO corrections is crucial to describe data within their experimental uncertainties.

Vector-boson pair production processes in particular have become an integral part of the rich precision programme at the LHC. Being measured by reconstructing the vector bosons from their leptonic decay products, those processes offer clean experimental signatures with rather small experimental uncertainties. Apart from the measurement of their production rates and distributions, they provide a proxy for both direct and indirect searches for beyond-the-SM (BSM) physics. While very precise SM predictions of diboson processes are not needed to find a light resonance structure in invariant-mass distributions, new-physics effects can give rise also to modifications and distortions of kinematic distributions. These effects can be parametrized through effective operators, such as anomalous triple-gauge couplings, and they enter vector-boson pair processes already at the leading order (LO). Constraining new-physics effects in these type of indirect searches crucially relies on accurate theory predictions for event rates and shapes of distributions.

$Z\gamma$ production in the $Z \to \ell^+\ell^-$ decay channel provides a particularly pure experimental signature as the final state can be fully reconstructed. In combination with its relatively large cross sections this process is well suited for precision phenomenology. Indeed, $Z\gamma$ production was measured extensively at the LHC at 7 TeV [38–43], 8 TeV [44–47], and 13 TeV [1, 48], and ref. [1] was the first diboson analysis to include the full Run II data set. Even small deviations from the production rate or distributions in this process would be a direct hint of BSM physics. So far, full agreement with the SM was found, which provides a strong test of the gauge structure of electroweak (EW) interactions and the mechanism of EW symmetry breaking. On the other hand, the measurement of a non-zero $ZZ\gamma$ coupling, which is absent in the SM, would be direct evidence of physics beyond the SM (BSM). Moreover, $Z\gamma$ final states are relevant in direct searches for BSM resonances and in Higgs boson measurements, see e.g. refs. [49, 50], with the SM production being an irreducible background. Although the Higgs decay into a $Z\gamma$ pair is rare, since it is loop induced in the SM, effects from new physics may significantly enhance this decay channel.

A substantial effort has been made in fixed-order calculations for $Z\gamma$ production in the past years. Next-to-leading order (NLO) QCD corrections were computed some time ago both for on-shell Z bosons [51] and including their leptonic decays [52]. The first contribution known at next-to-next-to-leading order (NNLO) QCD was the loop-induced gluon fusion contribution [53–55]. Ref. [56] combined the NLO cross section, including photon radiation off the leptons, with the loop-induced gluon fusion contribution. The full NNLO QCD cross section for $\ell^+\ell^-\gamma$ production was calculated in refs. [21, 22] at the fully differential level and it was later confirmed in ref. [23] by an independent calculation. Also the NLO electroweak (EW) corrections are known [57, 58].

However, the validity of fixed-order calculations is limited to observables dominated by hard QCD radiation. In kinematical regimes where soft and collinear QCD radiation becomes important, the perturbative expansion in the strong coupling constant is challenged by the appearance of large logarithmic contributions. The analytic resummation of those logarithms is usually restricted to a single observable, see e.g. the recent next-to-next-to-next-to-logarithmic (N³LL) results for the $Z\gamma$ transverse momentum ($p_{\text{T},\ell\ell\gamma}$) in refs. [59, 60] for instance, or at most two observables, such as the joint resummation of logarithms in $p_{\text{T},\ell\ell\gamma}$ and in the leading jet transverse momentum (p_{T,j_1}) at next-to-next-to-logarithmic (NNLL) [61]. Parton showers, on the other hand, offer a numerical approach to include all-order effects in all phase-space observables simultaneously. Although their all-order logarithmic accuracy is rather limited (see ref. [62] for a recent discussion on this topic), parton-shower simulations are extremely important for experimental analyses since they allow for an exclusive description of the final state. Moreover, as measurements operate at the level of hadronic events, they require full-fledged parton-shower Monte Carlo simulations. In fact, any BSM analysis searching for small deviations from SM predictions at event level requires parton-shower predictions that include the highest possible fixed-order accuracy. While matching of NLO QCD predictions and parton showers (NLO+PS) has been worked out a while ago in seminal papers [63–65],[1] current experimental measurements demand the inclusion of NNLO QCD corrections in event generators to fully exploit LHC data.

So far, four different NNLO+PS approaches have been presented in the literature [67–71], and all of them are formulated and applied for colour-singlet processes only. The methods of refs. [67, 70, 71] originate from the MINLO′ procedure [67, 72], which uses transverse-momentum resummation to upgrade a NLO calculation for colour singlet plus jet production to become NLO accurate for both zero-jet and one-jet observables. A numerical method that extends the MINLO′ procedure to higher jet multiplicities was presented in ref. [73], where in particular the case of Higgs production in association with up to two jets was worked out. NNLO+PS approaches have been mostly applied to the simple $2 \to 1$ LHC processes, such as Higgs-boson production [70, 71, 74, 75], the Drell-Yan process [69–71, 76, 77], and Higgs-strahlung [78–80], which in terms of QCD corrections is still a $2 \to 1$ process, and to the $H \to b\bar{b}$ decay [81, 82], which is a $1 \to 2$ process.

Up to now, only the approach of ref. [67], which relies on a numerically highly demanding multi-dimensional reweighting in the Born phase space, has been applied to a genuine $2 \to 2$ process, namely W^+W^- production [83].[2] This calculation has taken the reweighting procedure to its extreme. In fact, the Born phase space for $W^+W^- \to e^+\mu^-\nu_e\bar{\nu}_\mu$ involves nine variables (after taking the azimuthal symmetry into account). Ref. [83] had to resort to a number of features of the W-boson decays, such as the fact that the full angular dependence of each vector-boson decay can be parametrized through eight spherical

---

[1]For the processes considered in this work, in ref. [66] NLO QCD predictions for $Z\gamma$+jets with different jet multiplicities have been merged using the MEPS@NLO approach, which separates samples using a merging scale, and then interfaced to a parton shower.

[2]The W^+W^- NNLOPS simulation is based on the MINLO′ calculation of ref. [84], and the NNLO calculation of ref. [30] performed within the MATRIX framework [85].

harmonic functions [86], and used the fact that QCD corrections are largely independent of the off-shell-ness of the vector bosons to reduce the number of kinematic variables in the parametrization of the Born phase space. Still, the residual variables in the parametrization of the Born phase space need to be discretized. The finite bin sizes used in the reweighting limit the numerical accuracy of the results in regions of phase space that depend on coarse bins. This is typically the case close to kinematic edges and to boundaries of the phase space, such as tails of kinematic distributions, which, on the other hand, are particularly interesting for BSM searches. Actually, the numerical limitations related to an a-posteriori reweighting constitutes a problem already for the way simpler Drell-Yan process, since in this case, given the very large amount of data available, experiments require a high theoretical precision over the whole phase space.

In this paper, we consider $Z\gamma$ production and present the first NNLO+PS calculation for a genuine $2 \to 2$ process that includes NNLO QCD corrections directly during event generation, without any post-processing or reweighting of the events being required. In fact, this is also the first time a NNLO $Z\gamma$ calculation independent of a slicing cutoff is performed (cf. refs. [21–23]). To this end, we have extended the just recently developed MiNNLO$_{PS}$ method [70] to deal with genuine $2 \to 2$ reactions, which paves the way for NNLO+PS simulations of all other diboson processes. As anticipated already in ref. [70], MiNNLO$_{PS}$ is a very powerful approach as its underlying idea applies beyond $2 \to 1$ processes and beyond colour-singlet production, with the following features:

- NNLO corrections are calculated directly during the generation of the events, with no need for further reweighting.

- No merging scale is required to separate different multiplicities in the generated event samples.[3]

- When combined with transverse-momentum ordered parton showers, the matching preserves the leading logarithmic structure of the shower simulation.[4]

We consider all topologies leading to the final state $\ell^+\ell^-\gamma$ in our calculation, including off-shell effects and spin correlations. Since, neither a $Z\gamma$ nor a $Z\gamma$+jet generator was available within the POWHEG-BOX framework [87], we also present new calculations of these two processes using the POWHEG method [64]. Our implementation of the $Z\gamma$+jet generator builds the basis for the inclusion of NNLO QCD corrections to $Z\gamma$ production through the MiNNLO$_{PS}$ method. The ensuing calculation allows us to retain NNLO QCD accuracy in the event generation and to interface it to a parton shower, which is a necessary

---

[3]This concept was introduced and discussed in detail in ref. [67].

[4]We note that, while maintaining the logarithmic accuracy of the shower is sometimes taken for granted, this is instead a crucial and subtle point in any NNLO+PS approach. When MiNNLO$_{PS}$ predictions are interfaced to a transverse-momentum ordered shower, this requirement is automatically met, since the second-hardest emission is generated following the POWHEG matching procedure and the remaining ones by the parton shower. However, if the shower ordering variable differs from the one in the matching, maintaining the leading logarithmic accuracy of the shower can require the introduction of vetos to the shower radiation and of additional contributions, such as truncated showers [64].

step for a complete and realistic event simulation. In particular, multiple photon emissions through a QED shower, as well as non-perturbative QCD effects using hadronization and underlying event models can be included. These corrections can have a substantial impact on the lepton momenta, jet-binned cross sections and other more exclusive observables measured at the LHC.

This manuscript is organized as follows: in section 2 we discuss the implementation of $Z\gamma$ and $Z\gamma$+jet generators within the POWHEG-BOX-RES framework, where we introduce the two processes (section 2.1), recall some basics about POWHEG-BOX-RES (section 2.2), and give details on the treatment of photon isolation and the practical implementation (section 2.3). The inclusion of NNLO corrections to $Z\gamma$ production into the $Z\gamma$+jet generator is discussed in section 3, including details on the extraction of the two-loop amplitude (section 3.1), a general discussion on how we extended the MiNNLO$_{\rm PS}$ approach to $2 \to 2$ processes (section 3.2), and further practical details relevant for the specific case of the $Z\gamma$ MiNNLO$_{\rm PS}$ generator (section 3.3). In section 4, after describing the setup used in our calculation and the set of fiducial cuts used in the analysis (section 4.1), we first present results for fiducial cross sections (section 4.2), then a comparison of MiNNLO$_{\rm PS}$ with NNLO and MiNLO$'$ predictions (section 4.3), and with the most accurate prediction for the $Z\gamma$ transverse-momentum spectrum at NNLO+N^{3}LL (section 4.4), and finally we show how our predictions perform in comparison to ATLAS data at 13 TeV (section 4.5). We conclude and summarize in section 5. Some technical aspects are discussed in more detail in the appendices.

2   NLO+PS simulation of $Z\gamma$ and $Z\gamma$+jet production

In this section, we discuss the implementation of NLO+PS generators for $Z\gamma$ and $Z\gamma$+jet production in the POWHEG-BOX framework [87]. Both processes were not yet available in this framework and we present their first calculation in the POWHEG approach [65] at NLO+PS. Moreover, the $Z\gamma$+jet process serves as starting point to reach NNLO accuracy for $Z\gamma$ production through the MiNNLO$_{\rm PS}$ method, as detailed in section 3. Since these processes involve an EW resonance, we exploit the POWHEG-BOX-RES code [88], which is specifically designed to deal with intermediate resonances. In the following, we first introduce the two processes under consideration, then we recall some relevant features of the POWHEG-BOX-RES framework, and finally discuss details regarding the treatment of the photon in the final state and the QED singularities associated to it.

2.1   Description of the processes

We consider the production processes

$$pp \to \ell^+\ell^-\gamma \quad \text{and} \quad pp \to \ell^+\ell^-\gamma + \text{jet}\,, \tag{2.1}$$

where $\ell \in \{e, \mu\}$ is a massless charged lepton. For brevity, we refer to these processes as $Z\gamma$ and $Z\gamma$+jet production in the following.

As illustrated in figure 1, $Z\gamma$ production is initiated by quark-antiquark annihilation at LO. The photon can be emitted either by the quark line (q-type diagrams) or by the

a *q*-type diagram   b *ℓ*-type diagram
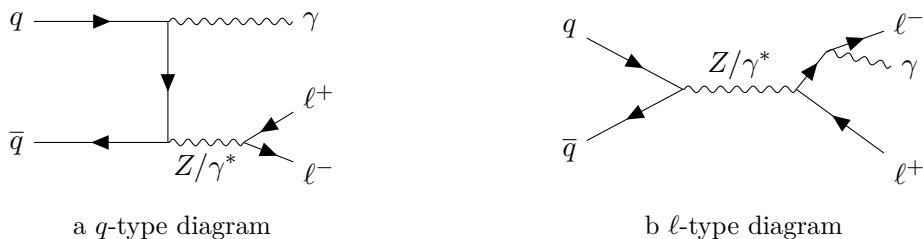
Figure 1. Sample LO diagrams for $\ell^+\ell^-\gamma$ production with two different resonance stuctures.

a   b

c

d   e
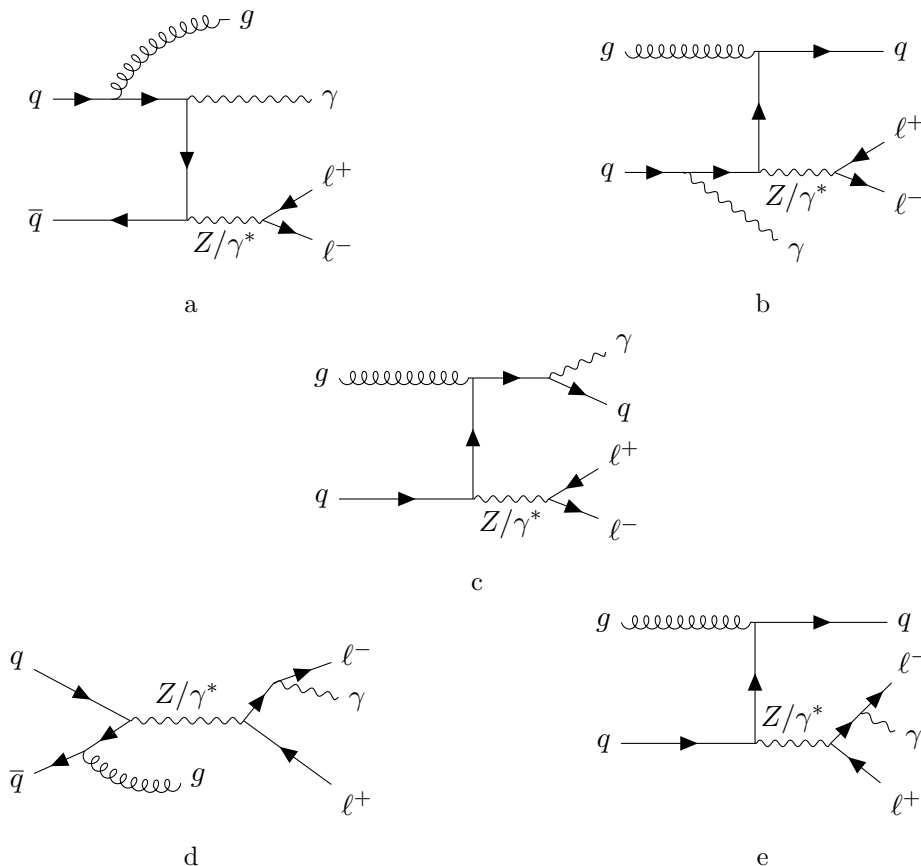
Figure 2. Sample LO diagrams for $\ell^+\ell^-\gamma$+jet production including *q*-type diagrams (a–c) and *ℓ*-type diagrams (d–e).

lepton line (*ℓ*-type diagrams), each of which yields a different resonance structure of the respective amplitudes. Sample LO diagrams for $Z\gamma$+jet production are shown in figure 2, with the same classification into *q*-type and *ℓ*-type diagrams. The distinction between those two resonance structures will be relevant when treating them as two different resonance histories within the POWHEG-BOX-RES framework, as discussed in section 2.2. In addition to the tree-level amplitudes at LO, the NLO calculation of the $Z\gamma$ ($Z\gamma$+jet) process requires the respective one-loop contributions as well as the tree-level real emission $Z\gamma$+jet ($Z\gamma$+2-jet) amplitudes.

The NLO corrections to $Z\gamma$ and $Z\gamma$+jet production have been implemented within the POWHEG-BOX-RES framework. For the $Z\gamma$ generator the relevant amplitudes have been extracted from MCFM [89], while for the $Z\gamma$+jet generator they have been implemented both using MCFM and via an interface to OPENLOOPS 2 [90–92]. The helicity amplitudes of MCFM are implemented from the analytic expressions computed in refs. [93, 94] for $Z\gamma$ production and in ref. [95] for $Z\gamma$+jet production. For the MCFM amplitudes of $Z\gamma$+jet production the contribution from third generation quarks inside the loops has been entirely removed for those diagrams where the Z boson is attached to a fermion loop through an axial vector coupling, while the massless bottom loop has been retained for those contributions where the corresponding top effects decouple as $1/m_{\text{top}}^4$ [23]. The impact of this approximation is expected to be rather small as shown in ref. [96], where the leading heavy-quark loop contribution has been evaluated in the $1/m_{\text{top}}^2$ expansion in the context of Z+jet and Z+2-jet production. We further note that, in view of the NNLO calculation for $Z\gamma$ production discussed in section 3, omitting the contribution of third generation quarks is in line with the fact that the heavy-quark loop contributions at two loop are currently not known, and therefore not included throughout our NNLO+PS results.

When using the OPENLOOPS interface for the NLO amplitudes of the $Z\gamma$+jet computation, the complex mass scheme can be exploited and the full top-mass effects can be accounted for, while in the MCFM amplitudes the width is implemented only in a fixed-width scheme and heavy-quark loop effects are included only approximately. Since QED effects are included just at LO, the difference between the complex-mass and the fixed-width scheme amounts to an overall normalization, whose impact is below 0.1%. When comparing results with full top-mass effects as available in OPENLOOPS to approximate results as implemented in MCFM we find per mille effects for quantities inclusive over QCD radiation. This is expected, since heavy-quark effects at one loop are non-vanishing only in the presence of final-state radiation. For jet-related quantities, the differences between the results, as shown in appendix C, are negligible at low transverse momentum and can range up to several tens of percent in the boosted region ($p_{\text{T}} \gtrsim m_{\text{top}}$). This is not surprising, since the process at hand involves s-channel fermion-loop contributions, which become more important in these phase space regions. For observables involving a jet our results are NLO accurate only, hence characterized by larger theoretical uncertainties. In summary, we find that mass effects are always much smaller than our quoted theoretical uncertainties and for the numerical studies performed in this paper, which are not devoted to boosted regions, using approximate results for the heavy-quark mass effects is justified. Hence, because of the better numerical performance of MCFM, we use the MCFM amplitudes to obtain all results of this paper. Specifically, we find that the MCFM virtual $Z\gamma$+jet amplitudes are about ten times faster than the OPENLOOPS ones. On the other hand, by making use of the folding option in POWHEG [87, 97], where the real contribution is evaluated multiple times for each virtual one, we could improve the numerical performance of the code using OPENLOOPS amplitudes. In fact, this is always the case when the virtual amplitudes constitute the bottleneck in the numerical evaluation. For greater flexibility, the release of the numerical code will include the option to choose between the OPENLOOPS and the MCFM implementations of the amplitudes.

2.2 The POWHEG-BOX-RES framework

We calculate NLO+PS predictions for $Z\gamma$ and $Z\gamma$+jet using the POWHEG method, which is based on the following master formula [64, 65, 87]:

$$\frac{\mathrm{d}\sigma}{\mathrm{d}\Phi_\mathrm{B}} = \bar{B}(\Phi_\mathrm{B}) \times \left\{ \Delta_\mathrm{pwg}(\Lambda_\mathrm{pwg}) + \int \mathrm{d}\Phi_\mathrm{rad} \Delta_\mathrm{pwg}(p_\mathrm{T,rad}) \frac{R(\Phi_\mathrm{B}, \Phi_\mathrm{rad})}{B(\Phi_\mathrm{B})} \right\}, \qquad (2.2)$$

where Φ_B is the Born phase space of the process under consideration. The function $\bar{B}(\Phi_\mathrm{B})$ describes the inclusive NLO process, where extra QCD emissions are integrated out; the content of the curly brackets is responsible for the exclusive generation of one extra QCD radiation with respect to the Born process according to the POWHEG method [64, 65, 87]. B and R denote the squared tree-level matrix elements for the process at Born level and for its real radiation, respectively. The evaluation of the POWHEG Sudakov form factor Δ_pwg [64] depends on the radiation phase space Φ_rad through the transverse momentum $p_\mathrm{T,rad}$ of the extra radiation. The POWHEG cutoff Λ_pwg is used to veto QCD emissions in the non-perturbative regime and its default value is $\Lambda_\mathrm{pwg} = 0.89\,\mathrm{GeV}$. The parton shower then adds additional radiation to eq. (2.2) that contributes beyond NLO with respect to the underlying Born process at all orders in perturbation theory. We refer to the original publications for explicit fomulae [64, 65, 87].

For the practical implementation of the $Z\gamma$ and $Z\gamma$+jet generators we exploit the POWHEG-BOX-RES framework [88], which takes into account the different resonance structures of each process. All possible resonance histories are automatically identified and the code performs a resonance-aware phase space sampling. When radiation from resonance decay products is considered (not done in the context of this paper), the efficiency of the infrared subtraction is improved by means of a resonance-aware subtraction algorithm, where the mapping from a real to the underlying Born configuration preserves the virtuality of intermediate resonances [88, 98]. Moreover, in a parton-shower context the distortion of resonances through recoil effects is avoided by supplying it with details on the resonance cascade chain.

The key idea behind the algorithm used in the POWHEG-BOX-RES framework is to decompose the cross section into contributions associated to a well-defined resonance structure, which are enhanced on that particular cascade chain. As discussed in section 2.1, both $Z\gamma$ and $Z\gamma$+jet production have two different resonance histories, which can be associated to q-type diagrams, where the photon is emitted from the quark/antiquark line, and ℓ-type ones, where the final state photon is radiated off one of the two leptons.

The POWHEG-BOX-RES framework takes as input *bare* flavour structures ℓ_B of the Born process (e.g. $\ell_\mathrm{B} = \{u\bar{u} \to \ell^+\ell^-\gamma\}$), which only contain the information on the initial- and final-state flavour structure. The full Born cross section can be written as the sum over all bare flavour structures of the corresponding Born contribution B_{ℓ_B}

$$B = \sum_{\ell_\mathrm{B}} B_{\ell_\mathrm{B}}. \qquad (2.3)$$

After introducing the *full* flavour and resonance structure $\hat{\ell}_\mathrm{B}$ of the Born process (e.g. $\hat{\ell}_\mathrm{B} = \{u\bar{u} \to Z \to \ell^+\ell^-\gamma\}$ or $\hat{\ell}_\mathrm{B} = \{u\bar{u} \to Z\gamma \to \ell^+\ell^-\gamma\}$), which embodies details on the

entire resonance history, we can further decompose $B_{\ell_{\mathrm{B}}}$ as a weighted sum over $\hat{\ell}_{\mathrm{B}}$ using weight functions $\mathcal{P}_{\hat{\ell}_{\mathrm{B}}}$

$$B_{\ell_{\mathrm{B}}} = \sum_{\hat{\ell}_{\mathrm{B}} \in T(\ell_{\mathrm{B}})} \mathcal{P}_{\hat{\ell}_{\mathrm{B}}} B_{\ell_{\mathrm{B}}}, \quad \text{with} \quad \sum_{\hat{\ell}_{\mathrm{B}} \in T(\ell_{\mathrm{B}})} \mathcal{P}_{\hat{\ell}_{\mathrm{B}}} = 1, \tag{2.4}$$

where $T(\ell_{\mathrm{B}})$ is named a *tree* and denotes all graphs with the given initial- and final-state flavour configuration ℓ_{B}. The weight functions $\mathcal{P}_{\hat{\ell}_{\mathrm{B}}}$ are chosen such that eq. (2.4) expresses $B_{\ell_{\mathrm{B}}}$ as a sum over resonance-peaked terms $\mathcal{P}_{\hat{\ell}_{\mathrm{B}}} B_{\hat{\ell}_{\mathrm{B}}}$, which develop the expected resonance enhancement of $\hat{\ell}_{\mathrm{B}}$. There is a certain freedom in their explicit expression, and in the POWHEG-BOX-RES code the following choice is made:

$$\mathcal{P}_{\hat{\ell}_{\mathrm{B}}} = \frac{P_{\hat{\ell}_{\mathrm{B}}}}{\sum_{\hat{\ell}'_{\mathrm{B}} \in T(\ell_{\mathrm{B}}(\hat{\ell}_{\mathrm{B}}))} P_{\hat{\ell}'_{\mathrm{B}}}}, \tag{2.5}$$

where the sum in the denominator runs over all configurations in the tree $T(\ell_{\mathrm{B}}(\hat{\ell}_{\mathrm{B}}))$ of graphs having a bare flavour structure $\ell_{\mathrm{B}}(\hat{\ell}_{\mathrm{B}})$ compatible with $\hat{\ell}_{\mathrm{B}}$. In the specific case of $Z\gamma$ and $Z\gamma$+jet production, $P_{\hat{\ell}_{\mathrm{B}}}$ assumes two different functional forms depending on whether $\hat{\ell}_{\mathrm{B}}$ refers to q-type or ℓ-type diagrams, and they read

$$P_{\hat{\ell}_{\mathrm{B}}} = \begin{cases} \dfrac{m_{\mathrm{Z}}^2}{(s_{\ell\ell} - m_{\mathrm{Z}}^2)^2 + \Gamma_{\mathrm{Z}}^2 m_{\mathrm{Z}}^2} & \hat{\ell}_{\mathrm{B}} \text{ is of } q\text{-type}, \\[3mm] \dfrac{m_{\mathrm{Z}}^2}{(s_{\ell\ell\gamma} - m_{\mathrm{Z}}^2)^2 + \Gamma_{\mathrm{Z}}^2 m_{\mathrm{Z}}^2} & \hat{\ell}_{\mathrm{B}} \text{ is of } \ell\text{-type}, \end{cases} \tag{2.6}$$

where $s_{\ell\ell}$ is the invariant mass of the lepton pair and $s_{\ell\ell\gamma}$ that of the $Z\gamma$ system. The same discussion applies to the virtual corrections, while for the real-emission contribution a similar decomposition is performed taking into account the different singular regions. As described in detail in ref. [88], the concept of resonance histories directly affects the definition of QCD singular regions: only soft/collinear singular regions compatible with a given full real flavour structure $\hat{\ell}_R$ are considered in the FKS decomposition of the real amplitude. It is important to note that, for each of the full real flavour structures $\hat{\ell}_R$ the mappings from the real to the Born configurations preserve the virtualities of the intermediate resonances, which is crucial to guarantee a cancellation of singularities between real corrections and their counterterms.

2.3 Treatment of the isolated photon and details of the implementation

The emission of a soft or collinear photon from a quark or a charged lepton induces QED singularities. Processes with final-state photons therefore require not only suitable criteria to isolate photons in the experimental analyses, but they also call for an IR-safe isolation procedure on the theory side. Since in the POWHEG-BOX framework fiducial cuts are usually applied at analyses level after parton showering, which modifies the kinematics of the final states, we discuss how to include photon-isolation requirements already at the event generation level in this framework to obtain IR-safe predictions.

To produce isolated photons in the final state there are two relevant mechanisms: the *direct* production in the hard process, which can be described perturbatively, and the production through *fragmentation* of a quark or a gluon, which is non-perturbative. The separation between the two production mechanisms in theoretical predictions is quite delicate, as sharply isolating the photon from the partons would spoil infrared (IR) safety. So-called *fragmentation functions* are required to absorb singularities related to collinear photon emissions in the latter production mechanism. Those functions are determined from data with relatively large uncertainties. On the other hand, Frixione's *smooth-cone isolation* of the photons [99] offers an IR-safe alternative that completely removes the fragmentation component. This substantially simplifies theoretical calculations of processes with isolated photons at higher orders in perturbation theory. Although the direct usage of smooth-cone isolation in experimental analyses is not possible due to the finite granularity of the calorimeter, data-theory comparisons are facilitated by tuning the smooth-cone parameters to mimic the fixed-cone isolation used by the experiments, see e.g. ref. [100].

So far, only few processes involving final-state photons have been implemented in the POWHEG-BOX framework: $W\gamma$ production [101] and direct photon production [98, 102]. These two generators make use of the photon fragmentation component. In particular in ref. [101] the hadron fragmentation into photons is modelled within POWHEG in combination with a QCD+QED shower. In this case the theoretical prediction can apply directly the photon isolation criteria imposed by the experiments to distinguish prompt photons taking part in the hard scattering process from possible background sources (such as photons from decay of π^0 mesons or from quark fragmentation). This facilitates a direct comparison between experimental and theoretical results. Those isolation criteria limit the hadronic activity in the vicinity of the photon by imposing

$$\sum_{\text{had}\in R_0} E_{\text{T}}^{\text{had}} < E_{\text{T}}^{\text{max}} \quad \text{with} \quad R_0 = \sqrt{\Delta\eta^2 + \Delta\phi^2}\,, \tag{2.7}$$

where the sum of the transverse energy $E_{\text{T}}^{\text{had}}$ of the hadrons inside a fixed cone of radius R_0 around the photon is constrained to be less than $E_{\text{T}}^{\text{max}}$.

In view of the NNLO extension considered in this paper, presented in section 3, we instead rely on smooth-cone isolation [99] to turn off the fragmentation component and to deal with QED collinear singularities perturbatively in an IR-safe manner. In this case, phase-space configurations where the photon becomes collinear to a quark are removed while preserving IR safety by allowing arbitrarily soft QCD radiation within smoothly decreasing cones around the photon direction. In practice, this means that the smooth-cone isolation is implemented by restricting the hadronic (partonic) activity within every cone of radius $\delta = \sqrt{(\Delta\eta)^2 + (\Delta\phi)^2} < \delta_0$ around a final-state photon, where δ_0 sets the maximal cone size, by imposing the following condition

$$\sum_{\text{had}/\text{part}\in\delta} E_{\text{T}}^{\text{had}/\text{part}} \leq E_{\text{T}}^{\text{max}}(\delta) = E_{\text{T}}^{\text{ref}}\left(\frac{1-\cos\delta}{1-\cos\delta_0}\right)^n, \qquad \forall\,\delta \leq \delta_0\,, \tag{2.8}$$

such that the total hadronic (partonic) transverse energy inside the cone is smaller than $E_{\text{T}}^{\text{max}}(\delta)$. The parameter n controls the smoothness of the isolation function and $E_{\text{T}}^{\text{ref}}$ is a

reference transverse-momentum scale that can be chosen to be either a fraction ϵ_γ of the transverse momentum of the respective photon ($p_{\mathrm{T},\gamma}$) or a fixed value (p_T^0),

$$E_\mathrm{T}^\mathrm{ref} = \epsilon_\gamma \, p_{\mathrm{T},\gamma} \qquad \text{or} \qquad E_\mathrm{T}^\mathrm{ref} = p_\mathrm{T}^0 \,. \tag{2.9}$$

In our calculations we impose smooth-cone isolation on the phase space of all $Z\gamma$+jet and $Z\gamma$+2-jet configurations. Furthermore, various technical phase-space cuts at event-generation level are necessary in order to obtain IR safe results. Those generation cuts and parameters of the smooth-cone isolation are given in appendix A. They are chosen to be much looser than the ones eventually applied at analyses level after parton showering. We stress that, since we also employ suppression factors for the NLO squared amplitudes (as discussed in detail below), the resulting differential cross section times suppression factors vanishes in the singular regions, which will not pass fiducial cuts.

As commonly used in many POWHEG-BOX generators, we exploit the possibility to split the real squared matrix element R into a singular and a finite (remnant) contribution. Such splitting improves the numerical performance of the code, especially as far as the efficiency of the event generation is concerned, in cases where the ratio R/B departs from its corresponding soft/collinear approximation, for instance in presence of Born zeros [103]. Following section 5 of ref. [87], we write the splitting into a singular and a remnant contribution for each singular region α of the real amplitude as:

$$R = \sum_\alpha R^\alpha(\Phi_\mathrm{R}) = \sum_\alpha \left[R_\mathrm{sing.}^\alpha(\Phi_\mathrm{R}) + R_\mathrm{remn.}^\alpha(\Phi_\mathrm{R}) \right] \,,$$
$$R_\mathrm{sing.}^\alpha(\Phi_\mathrm{R}) = \mathcal{S} R^\alpha(\Phi_\mathrm{R}) \,, \quad R_\mathrm{remn.}^\alpha(\Phi_\mathrm{R}) = (1-\mathcal{S}) R^\alpha(\Phi_\mathrm{R}) \,, \tag{2.10}$$

where Φ_R is the real phase-space and $\mathcal{S}$ is called *damping factor*. Only the singular contribution $\sum_\alpha R_\mathrm{sing.}^\alpha(\Phi_\mathrm{R})$ is exponentiated in the POWHEG Sudakov Δ_pwg and used to generate the first emission according to the POWHEG method in eq. (2.2), while the finite remnant contribution $\sum_\alpha R_\mathrm{remn.}^\alpha(\Phi_\mathrm{R})$ can be treated separately, by generating it with standard techniques and feeding it directly into the parton shower.

A standard damping factor [87] is used in both $Z\gamma$ and $Z\gamma$+jet generators, where $\mathcal{S}=0$ when the real squared amplitude in a singular region is greater than five times its soft/collinear approximation, and $\mathcal{S}=1$ otherwise. Additionally, to improve the numerical convergence, the $Z\gamma$+jet generator requires a special setting of the damping factor, which ensures that QED singularities appearing in the real squared matrix element are moved into the remnant contribution. Indeed, not all of the QED singular regions appearing in the real matrix elements have a singularity in their underlying Born amplitude. Accordingly, the associated real singularity is not mitigated by an overall Born suppression factor (as described in more detail below). To deal with this issue, we define, in each singular region, the invariant mass m_rad of the emitter-emitted pair of that singular region, which is the quantity that becomes small close to QCD singularities, and we use as a damping factor[5]

$$\mathcal{S}' = \frac{(m_\mathrm{rad}^2)^{-1}}{(m_\mathrm{rad}^2)^{-1} + c \sum_{i\in(q,\bar{q})} d_{i\gamma}^{-1}} \, \mathcal{S} \,, \tag{2.11}$$

---

[5]We thank Carlo Oleari for suggesting to absorb the QED singularities into the remnant contribution.

where $c \in [0, 1]$ is a free parameter that we choose below, and the sum runs over all (initial- and final-state) quarks with

$$\begin{aligned}
d_{i\gamma} &= p_{\mathrm{T},\gamma}^2 && \text{when } i \text{ is a quark in the initial state}\,, \\
d_{i\gamma} &= p_i \cdot p_\gamma && \text{when } i \text{ is a quark in the final state}\,.
\end{aligned} \tag{2.12}$$

The splitting induced by the suppression factor in eq. (2.11) is such that, when a QED singularity dominates, the event is included in $R^\alpha_{\mathrm{remn.}}(\Phi_{\mathrm{R}})$ ($\mathcal{S}' \to 0$), and, when the QCD singularity is dominant, the event is moved into $R^\alpha_{\mathrm{sing.}}(\Phi_{\mathrm{R}})$ ($\mathcal{S}' \to 1$). The numerical constant c controls the transition region between QED singularities in $d_{i\gamma}$ and QCD singularities in m_{rad}^2. Since $\alpha_{\mathrm{e}}/\alpha_{\mathrm{s}} \sim 0.1$, we use the value $c = 0.1$, which we have checked to be suitable for an efficient generation of events.

Finally, we exploit another tool of the POWHEG-BOX framework that allows us to improve the numerical convergence in the relevant phase-space regions. By introducing suppression factors, which multiply the cross section during integration and are a posteriori divided out again, it is possible to redirect the numerical sampling of events into certain regions in phase space. This is mandatory for processes that have singularities at Born level, such as the QED singularities in $Z\gamma$ and $Z\gamma$+jet production, to avoid sampling large statistics in phase-space regions which are eventually removed by the fiducial cuts at analysis level. In order to obtain suitable integration grids that give more weight to the phase-space regions selected by the fiducial cuts, we have introduced a Born suppression factor that vanishes in singular regions related both to QCD and QED emissions. Its precise form is given in appendix A. Since the real phase space is generated directly from the Born one in the POWHEG-BOX, the same factor is also applied to $R^\alpha_{\mathrm{sing.}}(\Phi_{\mathrm{R}})$. For the remnant contribution $R^\alpha_{\mathrm{remn.}}(\Phi_{\mathrm{R}})$, on the other hand, which is QCD regular, but is in our case QED singular, an analogous suppression factor has been chosen, that is given in appendix A as well.

We stress that the implementational details discussed throughout this section are by no means standard, despite the fact that the tools we are using existed already in the POWHEG-BOX framework. The proper adjustment of those tools and their related parameters required a great effort, which was necessary to obtain a generator for $Z\gamma$+jet production with sufficient numerical efficiency to be extended to NNLO corrections to $Z\gamma$ production discussed in the next section.

3 Reaching NNLO accuracy for $Z\gamma$ production using MiNNLO$_{\mathrm{PS}}$

We use our implementation of the $Z\gamma$+jet generator in the POWHEG-BOX-RES framework discussed in section 2 as a starting point. To include NNLO corrections for $Z\gamma$ production in this calculation we employ the recently developed MiNNLO$_{\mathrm{PS}}$ method [70]. To this end, we extend the MiNNLO$_{\mathrm{PS}}$ method to processes with non-trivial two-loop corrections, i.e. genuine $2 \to 2$ hard-scattering processes such as vector-boson pair production. After a general discussing of the ingredients required for a NNLO calculation, we recall the MiNNLO$_{\mathrm{PS}}$ method and present its extension to $2 \to 2$ processes. Finally, we pro-
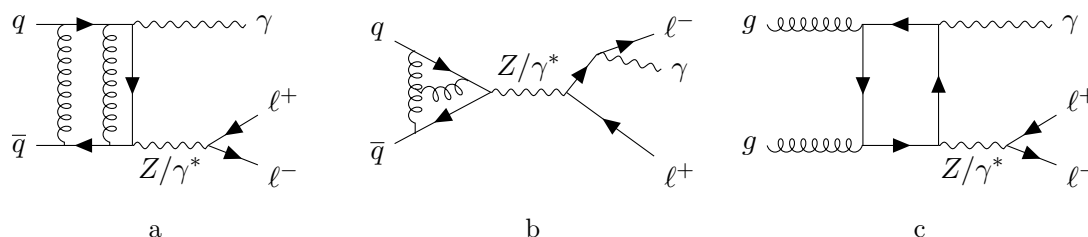
Figure 3. Sample Feynman diagrams entering the $\ell^+\ell^-\gamma$ process at NNLO: (a) q-type and (b) ℓ-type two-loop diagrams; (c) loop-induced gluon fusion contribution.

vide practical details on how that calculation is embedded in the POWHEG-BOX-RES framework.

3.1 Ingredients of a NNLO calculation

In section 2.1 we have discussed the contributions relevant to evaluate NLO corrections to $Z\gamma$ and $Z\gamma$+jet production. Those involve tree-level and one-loop amplitudes for the processes $pp \to Z\gamma$ and $pp \to Z\gamma$+jet as well as the tree-level amplitude for $pp \to Z\gamma$+2-jet. The same amplitudes enter the NNLO calculation for $Z\gamma$ production, i.e. at the Born level and as real, virtual one-loop, real-virtual and double-real corrections. The only missing ingredients for the NNLO calculation are the two-loop corrections in the $q\bar{q}$ channel, with sample diagrams shown in figure 3 (a-b), and the loop-induced contribution in the gluon-fusion channel, with a sample diagram shown in figure 3 (c). The latter is effectively only LO accurate and it can be separated from the others in a gauge-invariant way. Its size is rather small, being less than 10% of the NNLO corrections and below 1% of the full $Z\gamma$ cross section at NNLO [85]. We thus refrain from including the loop-induced gluon fusion contribution in our calculation. We note, however, that while its calculation at LO+PS is quite straightforward and easily done with current standard tools, see e.g. refs. [87, 104], a more sophisticated treatment would require to match the NLO corrections to the loop-induced gluon fusion contribution with parton showers. Despite being feasible with current technology, this is beyond the scope of this paper and left for future studies.

For the two-loop corrections we use the $q\bar{q} \to \ell\ell\gamma$ helicity amplitudes calculated in ref. [105]. Those have been fully implemented into the MATRIX framework [85, 106] using the results of ref. [105]. In order to exploit this implementation and evaluate the two-loop helicity amplitudes within our MiNNLO$_{\rm PS}$ calculation we have compiled MATRIX as a C++ library and linked it to our POWHEG-BOX-RES $Z\gamma$+jet generator.

We further exploit MATRIX for all fixed-order NNLO results used for comparisons throughout this paper. Through the recently implemented MATRIX+RADISH interface [59, 61, 107] the code now also combines NNLO calculations with high-accuracy resummation through the RADISH formalism [108–110] for different transverse observables, such as the transverse momentum of the colour singlet. We employ MATRIX+RADISH to obtain the $Z\gamma$ transverse momentum spectrum at NNLO+N^{3}LL for comparisons presented in section 4.

3.2 Generalization of MiNNLO$_{\text{PS}}$ to $2 \to 2$ colour-singlet processes

In the following we recall the central aspects of the MiNNLO$_{\text{PS}}$ method of ref. [70] as well as some of its improvements presented in ref. [71], and we discuss in detail all the changes required to apply the method to a genuine $2 \to 2$ colour-singlet process, such as vector-boson pair production. The main difference compared to $2 \to 1$ hadronic processes, such as Higgs and Drell-Yan production, is that the one- and two-loop virtual corrections for a general process can not be written as a simple form factor times the Born amplitude, and thereby receive a dependence on the respective flavour and phase-space configuration. To this end, we will recast, where appropriate, the relevant formulae of refs. [70, 71] in a flavour-dependent notation.

MiNNLO$_{\text{PS}}$ is a method to perform a NNLO calculation for a produced colour singlet F with invariant mass Q fully differential in the respective Born phase space Φ_{F}, in such a way that it can be subsequently matched to a parton shower. In the context of this paper F would be the $Z\gamma$ (or more precisely $\ell^+\ell^-\gamma$) final state, but we prefer to keep the discussion general throughout this section. We employ the same notation as in refs. [70, 71] in the following. The starting point of MiNNLO$_{\text{PS}}$ is a POWHEG implementation of colour-singlet production in association with one jet (FJ), whose phase space we denote by Φ_{FJ}. We thus write eq. (2.2) explicitly with the Born process being FJ production:

$$\frac{\mathrm{d}\sigma}{\mathrm{d}\Phi_{\text{FJ}}} = \bar{B}(\Phi_{\text{FJ}}) \times \left\{ \Delta_{\text{pwg}}(\Lambda_{\text{pwg}}) + \int \mathrm{d}\Phi_{\text{rad}} \Delta_{\text{pwg}}(p_{\text{T,rad}}) \frac{R(\Phi_{\text{FJ}}, \Phi_{\text{rad}})}{B(\Phi_{\text{FJ}})} \right\}. \tag{3.1}$$

Here, $\bar{B}(\Phi_{\text{FJ}})$ describes the FJ process, i.e. including the first radiation, using the full NLO cross section while the content of the curly brackets accounts for the second QCD emission through the POWHEG mechanism, with B and R being the squared tree-level matrix elements for FJ and FJJ production, respectively, and Φ_{rad} ($p_{\text{T,rad}}$) referring to the phase space (transverse momentum) of the second emission. Radiation beyond the second one is generated by the parton shower, which adds corrections of $\mathcal{O}(\alpha_s^3(Q))$ and higher at all orders in perturbation theory. In order to reach NNLO accuracy in the phase space of the color singlet F in eq. (3.1), we modify the content of the $\bar{B}(\Phi_{\text{FJ}})$ function, which is the central ingredient of the MiNNLO$_{\text{PS}}$ method.

The derivation of the $\bar{B}(\Phi_{\text{FJ}})$ function in MiNNLO$_{\text{PS}}$ [70] is based on the following formula that describes the transverse momentum of the color singlet (p_{T}) up to NNLO and is fully differential in the Born phase space Φ_{F}:

$$\frac{\mathrm{d}\sigma}{\mathrm{d}\Phi_{\text{F}}\mathrm{d}p_{\text{T}}} = \frac{\mathrm{d}}{\mathrm{d}p_{\text{T}}} \left\{ \sum_{\ell_{\text{F}}} \exp[-\tilde{S}_{\ell_{\text{F}}}(p_{\text{T}})] \mathcal{L}_{\ell_{\text{F}}}(p_{\text{T}}) \right\} + R_f(p_{\text{T}}) \tag{3.2}$$

$$= \sum_{\ell_{\text{F}}} \exp[-\tilde{S}_{\ell_{\text{F}}}(p_{\text{T}})] \, D_{\ell_{\text{F}}}(p_{\text{T}}) + R_f(p_{\text{T}}) \,,$$

where R_f includes only non-singular contributions at small p_{T}, and

$$D_{\ell_{\text{F}}}(p_{\text{T}}) \equiv -\frac{\mathrm{d}\tilde{S}_{\ell_{\text{F}}}(p_{\text{T}})}{\mathrm{d}p_{\text{T}}} \mathcal{L}_{\ell_{\text{F}}}(p_{\text{T}}) + \frac{\mathrm{d}\mathcal{L}_{\ell_{\text{F}}}(p_{\text{T}})}{\mathrm{d}p_{\text{T}}} \,. \tag{3.3}$$

At variance with the formulas in refs. [70, 71], we have introduced an explicit sum over the flavour structures ℓ_{F} of the Born process $pp \to \mathrm{F}$. The quantities without index ℓ_{F} should be understood as having been summed implicitly over ℓ_{F} as in the original formulation of refs. [70, 71]. Introducing the flavour sum in eq. (3.3) becomes necessary for a general colour-singlet process, because not only the luminosity factor $\mathcal{L}_{\ell_{\mathrm{F}}}$, but also the Sudakov form factor $\tilde{S}_{\ell_{\mathrm{F}}}(p_{\mathrm{T}})$ becomes flavour dependent. Their expressions read, cf. eqs. (4.31) and (2.9) of ref. [70],[6]

$$
\mathcal{L}_{\ell_{\mathrm{F}}=cc'}(p_{\mathrm{T}}) = \sum_{i,j} \left\{ \left(\tilde{C}_{ci}^{[a]} \otimes f_i^{[a]} \right) \frac{\mathrm{d}\left[|M^{\mathrm{F}}|_{cc'}^2 \tilde{H}_{\ell_{\mathrm{F}}=cc'}(p_{\mathrm{T}}) \right]}{\mathrm{d}\Phi_{\mathrm{F}}} \left(\tilde{C}_{c'j}^{[b]} \otimes f_j^{[b]} \right) \right.
$$
$$
\left. + \left(G_{ci}^{[a]} \otimes f_i^{[a]} \right) \frac{\mathrm{d}\left[|M^{\mathrm{F}}|_{cc'}^2 \tilde{H}_{\ell_{\mathrm{F}}=cc'}(p_{\mathrm{T}}) \right]}{\mathrm{d}\Phi_{\mathrm{F}}} \left(G_{c'j}^{[b]} \otimes f_j^{[b]} \right) \right\}, \tag{3.4}
$$

$$
\tilde{S}_{\ell_{\mathrm{F}}}(p_{\mathrm{T}}) = 2 \int_{p_{\mathrm{T}}}^{Q} \frac{\mathrm{d}q}{q} \left(A(\alpha_s(q)) \ln \frac{Q^2}{q^2} + \tilde{B}_{\ell_{\mathrm{F}}}(\alpha_s(q)) \right), \tag{3.5}
$$

with

$$
A(\alpha_s) = \left(\frac{\alpha_s}{2\pi} \right) A^{(1)} + \left(\frac{\alpha_s}{2\pi} \right)^2 A^{(2)} + \left(\frac{\alpha_s}{2\pi} \right)^3 A^{(3)},
$$
$$
\tilde{B}_{\ell_{\mathrm{F}}}(\alpha_s) = \left(\frac{\alpha_s}{2\pi} \right) B^{(1)} + \left(\frac{\alpha_s}{2\pi} \right)^2 \tilde{B}_{\ell_{\mathrm{F}}}^{(2)}. \tag{3.6}
$$

The flavour dependence of these quantities originates entirely from the hard-virtual coefficient function $H_{\ell_{\mathrm{F}}}$,[7] which contains the virtual corrections that, for a general $2 \to 2$ hadronic process, become dependent on the flavour and on the Born phase-space Φ_{F}. Up to two loops it is given by

$$
H_{\ell_{\mathrm{F}}}(p_{\mathrm{T}}) = 1 + \left(\frac{\alpha_s(p_{\mathrm{T}})}{2\pi} \right) H_{\ell_{\mathrm{F}}}^{(1)} + \left(\frac{\alpha_s(p_{\mathrm{T}})}{2\pi} \right)^2 H_{\ell_{\mathrm{F}}}^{(2)}. \tag{3.7}
$$

This dependence propagates through the $\tilde{B}_{\ell_{\mathrm{F}}}^{(2)}$ coefficient to the Sudakov form factor, since the derivation of the MiNNLO$_{\mathrm{PS}}$ formalism is based on setting the renormalization scale $\mu_{\mathrm{R}} \sim p_{\mathrm{T}}$, which exponentiates the $H_{\ell_{\mathrm{F}}}^{(1)}$ coefficient and requires a redefinition of $B_{\ell_{\mathrm{F}}}^{(2)}$, as discussed in the derivation of the replacement in eq. (4.26) of ref. [70]:

$$
\tilde{B}_{\ell_{\mathrm{F}}}^{(2)} = B^{(2)} + 2\zeta_3 (A^{(1)})^2 + 2\pi\beta_0 H_{\ell_{\mathrm{F}}}^{(1)}, \tag{3.8}
$$

where $\beta_0 = \frac{11C_{\mathrm{A}} - 2N_{\mathrm{f}}}{12\pi}$. A few comments are in order: all quantities with index ℓ_{F} also depend on the Born kinematics. For ease of notation we do not indicate explicitly their Φ_{F} dependence. The G functions [111] in eq. (3.4) are present only in the case of gluon-induced reactions, i.e. they are zero for $Z\gamma$ production and kept here only for completeness. For a colour-singlet process the Born flavours ℓ_{F} correspond to the two initial-state partons, which have been denoted with cc' in eq. (3.4). In that equation $|M^{\mathrm{F}}|_{cc'}^2$ denotes the Born matrix

---

[6]The convolution between two functions $f(z)$ and $g(z)$ is defined as $(f \otimes g)(z) \equiv \int_z^1 \frac{\mathrm{d}x}{x} f(x) g\left(\frac{z}{x} \right)$.

[7]Note that $\tilde{H}_{\ell_{\mathrm{F}}}$ in eq. (3.4) just includes an additional shift with respect to $H_{\ell_{\mathrm{F}}}$, see eq. (4.26) of ref. [70].

element squared, $\tilde{C}$ are the collinear coefficient functions, and $f_{i/j}^{[a/b]}$ are the parton densities. A crucial feature of MiNNLO$_{\rm PS}$ is that both the renormalization and the factorization scales are set to $\mu_{\rm R} \sim \mu_{\rm F} \sim p_{\rm T}$. The precise definition of the first- and second-order hard functions $H_{\ell_{\rm F}}^{(1)}$ and $H_{\ell_{\rm F}}^{(2)}$ is given in section 3.3.

Writing also the differential NLO cross section for FJ production as a sum over its flavour structures $\ell_{\rm FJ}$

$$\frac{{\rm d}\sigma_{\rm FJ}^{\rm (NLO)}}{{\rm d}\Phi_{\rm F}{\rm d}p_{\rm T}} = \sum_{\ell_{\rm FJ}} \left\{ \frac{\alpha_s(p_{\rm T})}{2\pi} \left[\frac{{\rm d}\sigma_{\rm FJ}}{{\rm d}\Phi_{\rm F}{\rm d}p_{\rm T}}\right]_{\ell_{\rm FJ}}^{(1)} + \left(\frac{\alpha_s(p_{\rm T})}{2\pi}\right)^2 \left[\frac{{\rm d}\sigma_{\rm FJ}}{{\rm d}\Phi_{\rm F}{\rm d}p_{\rm T}}\right]_{\ell_{\rm FJ}}^{(2)} \right\}, \qquad (3.9)$$

where $[X]^{(i)}$ denotes the coefficient of the $i^{\rm th}$ term in the perturbative expansion of the quantity X, allows us to recast our starting formula in eq. (3.2) as

$$\frac{{\rm d}\sigma}{{\rm d}\Phi_{\rm F}{\rm d}p_{\rm T}} = \sum_{\ell_{\rm FJ}} \left\{ \exp[-\tilde{S}_{\ell_{\rm F}\leftarrow\ell_{\rm FJ}}(p_{\rm T})] \left\{ \frac{\alpha_s(p_{\rm T})}{2\pi} \left[\frac{{\rm d}\sigma_{\rm FJ}}{{\rm d}\Phi_{\rm F}{\rm d}p_{\rm T}}\right]_{\ell_{\rm FJ}}^{(1)} \left(1 + \frac{\alpha_s(p_{\rm T})}{2\pi}[\tilde{S}_{\ell_{\rm F}\leftarrow\ell_{\rm FJ}}(p_{\rm T})]^{(1)}\right) \right.\right.$$
$$\left.\left. + \left(\frac{\alpha_s(p_{\rm T})}{2\pi}\right)^2 \left[\frac{{\rm d}\sigma_{\rm FJ}}{{\rm d}\Phi_{\rm F}{\rm d}p_{\rm T}}\right]_{\ell_{\rm FJ}}^{(2)} \right\} \right\} + \sum_{\ell_{\rm F}} \exp[-\tilde{S}_{\ell_{\rm F}}(p_{\rm T})]\, \mathcal{D}_{\ell_{\rm F}}(p_{\rm T})$$
$$+ \text{ regular terms of } \mathcal{O}(\alpha_{\rm s}^3)\,, \qquad (3.10)$$

where $\ell_{\rm F} \leftarrow \ell_{\rm FJ}$ denotes the projection from the flavour structure of FJ production to the one of the Born process F. This projection is trivial in the case of $Z\gamma$ production, as the Born is always $q\bar{q}$ initiated and only the respective quark-flavour is of relevance in the $\ell_{\rm F}$ dependence of $\tilde{S}_{\ell_{\rm F}}(p_{\rm T})$. Note that the evaluation of $\exp[-\tilde{S}_{\ell_{\rm F}\leftarrow\ell_{\rm FJ}}(p_{\rm T})]$ also requires a projection for $\Phi_{\rm FJ} \to \Phi_{\rm F}$ as discussed below. Furthermore, we have introduced a new symbol $\mathcal{D}_{\ell_{\rm F}}(p_{\rm T})$ that accounts for the relevant NNLO corrections with the following two choices of treating terms beyond accuracy. In the original MiNNLO$_{\rm PS}$ formulation of ref. [70] we have truncated eq. (3.10) to third order in $\alpha_s(p_{\rm T})$, i.e.

$$\mathcal{D}_{\ell_{\rm F}}(p_{\rm T}) \equiv \left(\frac{\alpha_s(p_{\rm T})}{2\pi}\right)^3 [D_{\ell_{\rm F}}(p_{\rm T})]^{(3)} + \mathcal{O}(\alpha_s^4)\,. \qquad (3.11)$$

With this truncation at the differential level eq. (3.10) does not reproduce anymore the exact total derivative that we started with in eq. (3.2). In order to preserve the total derivative and keep into account additional terms beyond accuracy, a new prescription has been suggested in ref. [71]

$$\mathcal{D}_{\ell_{\rm F}}(p_{\rm T}) \equiv D_{\ell_{\rm F}}(p_{\rm T}) - \frac{\alpha_s(p_{\rm T})}{2\pi}[D_{\ell_{\rm F}}(p_{\rm T})]^{(1)} - \left(\frac{\alpha_s(p_{\rm T})}{2\pi}\right)^2 [D_{\ell_{\rm F}}(p_{\rm T})]^{(2)}\,, \qquad (3.12)$$

which will be our default choice throughout this paper. The relevant expressions for its evaluation, including the ones of the $[D_{\ell_{\rm F}}(p_{\rm T})]^{(i)}$ coefficients, are reported in appendix C and D of ref. [70] and in appendix A of ref. [71], where the flavour dependence can be simply included through the replacements $H^{(1)} \to H_{\ell_{\rm F}}^{(1)}$, $H^{(2)} \to H_{\ell_{\rm F}}^{(2)}$, and $\tilde{B}^{(2)} \to \tilde{B}_{\ell_{\rm F}}^{(2)}$. As discussed in detail in refs. [70, 71], eq. (3.10) is NNLO accurate upon integration over

p_{T}, through the consistent inclusion of all singular terms to third order in $\alpha_s(p_{\mathrm{T}})$. This is achieved with both choices of $\mathcal{D}_{\ell_{\mathrm{F}}}(p_{\mathrm{T}})$, as they differ only by terms of $\mathcal{O}(\alpha_s^4)$ and higher.

We can now make the connection to POWHEG and the parton-shower matching formula in eq. (3.1). The formulation of eq. (3.10) applies also to the fully differential cross section in the Φ_{FJ} phase space, and it can be used to achieve NNLO accuracy for the $\bar{B}(\Phi_{\mathrm{FJ}})$ function [70, 71]

$$
\bar{B}(\Phi_{\mathrm{FJ}}) \equiv \sum_{\ell_{\mathrm{FJ}}} \left\{ \exp[-\tilde{S}_{\ell_{\mathrm{F}} \leftarrow \ell_{\mathrm{FJ}}}(p_{\mathrm{T}})] \left\{ \frac{\alpha_s(p_{\mathrm{T}})}{2\pi} \left[\frac{\mathrm{d}\sigma_{\mathrm{FJ}}}{\mathrm{d}\Phi_{\mathrm{FJ}}} \right]^{(1)}_{\ell_{\mathrm{FJ}}} \left(1 + \frac{\alpha_s(p_{\mathrm{T}})}{2\pi} [\tilde{S}_{\ell_{\mathrm{F}} \leftarrow \ell_{\mathrm{FJ}}}(p_{\mathrm{T}})]^{(1)} \right) \right.\right.
$$
$$
\left.\left. + \left(\frac{\alpha_s(p_{\mathrm{T}})}{2\pi} \right)^2 \left[\frac{\mathrm{d}\sigma_{\mathrm{FJ}}}{\mathrm{d}\Phi_{\mathrm{FJ}}} \right]^{(2)}_{\ell_{\mathrm{FJ}}} \right\} + \left\{ \sum_{\ell_{\mathrm{F}}} \exp[-\tilde{S}_{\ell_{\mathrm{F}}}(p_{\mathrm{T}})] \, \mathcal{D}_{\ell_{\mathrm{F}}}(p_{\mathrm{T}}) \right\} F^{\mathrm{corr}}_{\ell_{\mathrm{FJ}}}(\Phi_{\mathrm{FJ}}) \right\},
$$
$$
\tag{3.13}
$$

where $F^{\mathrm{corr}}_{\ell_{\mathrm{FJ}}}(\Phi_{\mathrm{FJ}})$ guarantees a proper spreading of the Born-like NNLO corrections in the full Φ_{FJ} phase space, as discussed in detail in section 3 of ref. [70] and briefly recalled in the next section. One should bear in mind that there is an implicit dependence on Φ_{F} of all quantities that depend on ℓ_{F}. To obtain the respective kinematics requires a suitable projection $\Phi_{\mathrm{FJ}} \to \Phi_{\mathrm{F}}$, see section 3.3 and in appendix B (cf. also appendix A of ref. [70]).

3.3 Practical details of the implementation within POWHEG-BOX-RES

We have applied the MiNNLO$_{\mathrm{PS}}$ formalism discussed in the previous section to our implementation of the $Z\gamma$+jet generator in POWHEG-BOX-RES. In the following we discuss practical aspects of our calculation in that framework and set F $= Z\gamma$ from now on.

We briefly recall how the NNLO corrections, which have Born kinematics and additionally depend on p_{T}, are included in $Z\gamma$+jet generator. The relevant kinematics is obtained by performing a phase-space projection $\Phi_{Z\gamma J} \to \Phi_{Z\gamma}$ and by determining p_{T} from the given $\Phi_{Z\gamma J}$ phase-space point. Furthermore, the Born-like NNLO corrections need to be distributed in the $\Phi_{Z\gamma J}$ kinematics. There is a certain degree of freedom in how to associate $(\Phi_{Z\gamma}, p_{\mathrm{T}})$ with the full $\Phi_{Z\gamma J}$ phase space. This is encoded in the factor $F^{\mathrm{corr}}(\Phi_{Z\gamma J})$ of eq. (3.13)

$$
F^{\mathrm{corr}}(\Phi_{Z\gamma J}) = \frac{J_{\ell_{Z\gamma J}}(\Phi_{Z\gamma J})}{\sum_{\ell'_{Z\gamma J}} \int \mathrm{d}\Phi'_{Z\gamma J} J_{\ell'_{Z\gamma J}}(\Phi'_{Z\gamma J}) \delta(p_{\mathrm{T}} - p'_{\mathrm{T}}) \delta(\Phi_{Z\gamma} - \Phi'_{Z\gamma})} \,, \tag{3.14}
$$

and in the details of the $\Phi_{Z\gamma J} \to \Phi_{Z\gamma}$ projection. The functions $J_{\ell_{Z\gamma J}}(\Phi_{\mathrm{FJ}})$ for $\ell_{Z\gamma J} = \{q\bar{q}, qg, gq\}$ have been chosen according to the collinear limit of the tree-level matrix element squared of the $Z\gamma$+jet process, using eq. (A.14) of ref. [70]. This is a suitable compromise between computational speed and physically sound results, as the spreading is performed according to the pseudorapidity distribution of the radiation described by that approximation. With this choice the numerical convergence of the integral in the denominator of eq. (3.14) does not scale with the complexity of the process, which is a crucial requirement for multi-leg processes, such as the one at hand. We stress that the spreading factor in eq. (3.14) is designed in such a way that the integral over the $\Phi_{Z\gamma J}$ phase space

of its product with any function that depends on $\Phi_{Z\gamma}$ yields exactly the integral of that function when integrated over the $\Phi_{Z\gamma}$ phase space, see eq. (3.2) of ref. [70].

We provide some details on our choice for the $\Phi_{Z\gamma J} \to \Phi_{Z\gamma}$ projection in appendix B (cf. also appendix A of ref. [70]). Note that this projection does not preserve the full Born kinematics. While it keeps all invariant masses and the rapidity of the $Z\gamma$ system unchanged, it does alter for instance the transverse momentum of the photon. As a result, the photon transverse momentum after the $\Phi_{Z\gamma J} \to \Phi_{Z\gamma}$ projection is neither bounded from below by the technical generation cuts nor controlled by the phase-space suppression factor introduced for the $\Phi_{Z\gamma J}$ kinematics in section 2.3. This induces a singular behaviour through the Born and virtual amplitudes in both the Sudakov form factor and the luminosity factor defined in eqs. (3.4) and (3.5). We have therefore added the requirement $p_{\mathrm{T},\gamma} \geq 10\,\mathrm{GeV}$ in the projected $\Phi_{Z\gamma}$ kinematics. This technical cut is below the $p_{\mathrm{T},\gamma}$ threshold used at analysis level and it can be controlled through the input card. Its effect is strictly beyond accuracy, affecting only regular contributions at large $p_{\mathrm{T},\ell\ell\gamma}$. In fact, as discussed in appendix B, our projection can lead to configurations with $p_{\mathrm{T},\gamma} \to 0$ only for events where the jet is back to back to the $Z\gamma$ system, and the Z and the photon are aligned with each other. It is then clear that $p_{\mathrm{T},j} > p_{\mathrm{T},\gamma}$ for such events and that there are no large logarithms associated to $p_{\mathrm{T},j}$. Indeed, we have varied the cutoff down by a factor of ten, finding changes at the level of the numerical precision of less than a 1%.

Embedding the MiNNLO$_{\mathrm{PS}}$ corrections within the POWHEG-BOX-RES framework requires some further discussion with respect to the resonance-aware features. Since the $\bar{B}(\Phi_{Z\gamma})$ function is modified in an additive way in eq. (3.13), such that the NNLO corrections are treated on the same footing as all other contributions with $\Phi_{Z\gamma J}$ kinematics, we decompose them as a weighted sum over $\hat{\ell}_{\mathrm{B}}$ using the weight functions $\mathcal{P}_{\hat{\ell}_{\mathrm{B}}}$ just like in eq. (2.4). Our final formula for the $Z\gamma$ MiNNLO$_{\mathrm{PS}}$ generator reads

$$
\begin{aligned}
\bar{B}(\Phi_{Z\gamma J}) \equiv \sum_{\ell_{Z\gamma J}} & \left\{ \exp[-\tilde{S}_{\ell_{Z\gamma} \leftarrow \ell_{Z\gamma J}}(p_{\mathrm{T}})] \left\{ \frac{\alpha_s(p_{\mathrm{T}})}{2\pi} \left[\frac{\mathrm{d}\sigma_{Z\gamma J}}{\mathrm{d}\Phi_{Z\gamma J}} \right]^{(1)}_{\ell_{Z\gamma J}} \left(1 + \frac{\alpha_s(p_{\mathrm{T}})}{2\pi} [\tilde{S}_{\ell_{Z\gamma} \leftarrow \ell_{Z\gamma J}}(p_{\mathrm{T}})]^{(1)} \right) \right. \right. \\
& \left. + \left(\frac{\alpha_s(p_{\mathrm{T}})}{2\pi} \right)^2 \left[\frac{\mathrm{d}\sigma_{Z\gamma J}}{\mathrm{d}\Phi_{Z\gamma J}} \right]^{(2)}_{\ell_{Z\gamma J}} \right\} \\
& \left. + \sum_{\hat{\ell}_{Z\gamma} \in T(\ell_{Z\gamma J})} \mathcal{P}_{\hat{\ell}_{Z\gamma J}} \left\{ \sum_{\ell_{Z\gamma}} \exp[-\tilde{S}_{\ell_{Z\gamma}}(p_{\mathrm{T}})] \, \mathcal{D}_{\ell_{Z\gamma}}(p_{\mathrm{T}}) \right\} F^{\mathrm{corr}}_{\ell_{Z\gamma J}}(\Phi_{Z\gamma J}) \right\}.
\end{aligned}
\tag{3.15}
$$

In the following we provide some details on the treatment of higher-order terms and the scale settings. The discussion summarizes briefly the one in section 3.2 of ref. [71], which we refer to for more details. In the large transverse-momentum region it is important to switch off higher-order logarithmic terms to avoid spurious contributions. As is standard, we do this by introducing modified logarithms via the replacement

$$
\log\left(\frac{Q}{p_{\mathrm{T}}} \right) \to L \equiv \frac{1}{p} \log\left(1 + \left(\frac{Q}{p_{\mathrm{T}}} \right)^p \right),
\tag{3.16}
$$

with the setting $p = 6$. As pointed out in ref. [71], in order to preserve the total derivative of eq. (3.2), this prescription requires three further adjustments. The lower integration

bound of the Sudakov is to be replaced by $p_{\mathrm{T}} \to Q e^{-L}$; $\mathcal{D}_{\ell_{\mathrm{F}}}(p_{\mathrm{T}})$ (or $\mathcal{D}_{\ell_{\mathrm{F}}}(p_{\mathrm{T}})^{(3)}$) needs to be multiplied by a proper jacobian factor, see eqs. (13) and (16) of ref. [71]; the perturbative scales need to be set consistently with the scale of the modified logarithms at small transverse momenta. Additionally, we smoothly approach non-perturbative scales at small p_{T} and introduce the non-perturbative parameter Q_0 to regularize the Landau singularity, setting the central renormalization and factorization scales to [71]

$$\mu_{\mathrm{R},0} = Q e^{-L} + Q_0 \, g(p_{\mathrm{T}}) \,, \qquad \mu_{\mathrm{F},0} = Q e^{-L} + Q_0 \, g(p_{\mathrm{T}}) \,, \tag{3.17}$$

where we set $Q_0 = 0.5\,\mathrm{GeV}$, and $g(p_{\mathrm{T}})$ is chosen such that it suppresses the Q_0 shift at large values of p_{T}:

$$g(p_{\mathrm{T}}) = \left(1 + \frac{Q}{Q_0} e^{-L} \right)^{-1} \,. \tag{3.18}$$

The scale setting of eq. (3.17) provides a consistent treatment in the small p_{T} region and preserves the total derivative of eq. (3.2). However, at large p_{T} it yields $\mu_{\mathrm{R},0} \sim \mu_{\mathrm{F},0} \sim Q$, while a scale setting of $\mu_{\mathrm{R},0} \sim \mu_{\mathrm{F},0} \sim p_{\mathrm{T}}$ might be preferred in that region. To this end, the scales entering the NLO $Z\gamma$+jet cross section in eq. (3.15) can be set in the input card (`largeptscales 1`) to

$$\mu_{\mathrm{R},0} = p_{\mathrm{T}} + Q_0 \, g(p_{\mathrm{T}}) \,, \qquad \mu_{\mathrm{F},0} = p_{\mathrm{T}} + Q_0 \, g(p_{\mathrm{T}}) \,, \tag{3.19}$$

which we apply in our calculation. It is important that eq. (3.19) matches the scales of the Sudakov form factor and the $\mathcal{D}_{\ell_{\mathrm{F}}}(p_{\mathrm{T}})$ terms at small p_{T}. At the same time it ensures a dynamical scale choice of $\mu_{\mathrm{R},0} = \mu_{\mathrm{F},0} \sim p_{\mathrm{T}}$ at large p_{T}.

Next, we specify the precise definition of the first and second order hard-virtual function of eq. (3.7) for $Z\gamma$ production in our subtraction scheme. First, let us recall that all tree-level and one-loop amplitudes have been extracted from MCFM and for comparison also linked through OPENLOOPS, and that the (one-loop and) two-loop $q\bar{q} \to \ell\ell\gamma$ amplitudes have been obtained by creating an interface to their implementation in MATRIX. At variance with the $2 \to 1$ processes considered in refs. [70, 71], it is not possible to provide compact expressions for the hard function of $Z\gamma$ production. For brevity, we thus start from the expressions of the first and second order hard-virtual function where IR singularities have been subtracted according to the q_T-*scheme* (more precisely, choosing the *hard-scheme* [112] as resummation scheme) that we denote as $H_{\ell_{\mathrm{F}}}^{q_{\mathrm{T}}(1)}$ and $H_{\ell_{\mathrm{F}}}^{q_{\mathrm{T}}(2)}$ in the following. Those coefficients are unambiguously defined in eqs. (12) and (62) of ref. [112] and can be extracted from the one-loop and two-loop virtual amplitudes using the expressions of that paper. In fact, the MATRIX interface directly provides the hard-virtual coefficients in that scheme, so that we only need to perform the appropriate scheme conversion to match the MiNNLO$_{\mathrm{PS}}$ conventions [113]:[8]

$$H_{\ell_{\mathrm{F}}=cc'}^{(1)} = H_{\ell_{\mathrm{F}}=cc'}^{q_{\mathrm{T}}(1)} - 2C_{cc}^{(1),\delta} \,, \tag{3.20}$$

$$H_{\ell_{\mathrm{F}}=cc'}^{(2)} = H_{\ell_{\mathrm{F}}=cc'}^{q_{\mathrm{T}}(2)} - (C_{cc}^{(1),\delta})^2 + 2C_{cc}^{(2),\delta} - 2C_{cc}^{(1),\delta}(H_{\ell_{\mathrm{F}}=cc'}^{q_{\mathrm{T}}(1)} - 2C_{cc}^{(1),\delta}) \tag{3.21}$$

---

[8]This scheme conversion follows directly from the fact that the hard-scheme is defined in ref. [112] such that the collinear coefficient functions do not contain any $\delta(1-z)$ terms, which are absorbed into $H_{\ell_{\mathrm{F}}}^{q_{\mathrm{T}}}$ instead.

where $C_{cc'}^{(1),\delta}$ and $C_{cc'}^{(2),\delta}$ are the terms proportional to $\delta(1-z)$ of the first and second order coefficients of the collinear coefficient functions, which in the case of a quark-induced process ($cc' = q\bar{q}$) are given by

$$\tilde{C}_{qq}^{(1),\delta} = -C_F \frac{\pi^2}{24}\,, \tag{3.22}$$

$$\tilde{C}_{qq}^{(2),\delta} = \frac{9C_F^2\pi^4 + 2C_A C_F(4856 - 603\pi^2 + 18\pi^4 - 2772\zeta_3) + 4N_f C_F(-328 + 45\pi^2 + 252\zeta_3)}{10368}\,, \tag{3.23}$$

where $C_F = 4/3$ and $C_A = 3$, and N_f is the number of light quark flavours. Note that $\tilde{C}_{qq}^{(1/2)}$ in the MiNNLO$_{PS}$ convention can be obtained from the ones of ref. [112] by simply adding $\tilde{C}_{qq}^{(1/2),\delta} \times \delta(1-z)$. For completeness, we also provide the corresponding expressions for the gluon-induced case ($cc' = gg$)

$$\tilde{C}_{gg}^{(1),\delta} = -C_A \frac{\pi^2}{24}\,, \tag{3.24}$$

$$\begin{aligned}
\tilde{C}_{gg}^{(2),\delta} = {}& -\frac{10718}{864} - \frac{5C_A}{192} - \frac{C_F}{24} + \frac{9C_F^2}{8} - \frac{1679\pi^2}{192} - \frac{37\pi^4}{64} + C_A C_F\left(-\frac{145}{48} - \frac{7\pi^2}{16}\right) \\
& + C_A^2\left(\frac{3187}{576} + \frac{43\pi^2}{36} + \frac{79\pi^4}{1152} - \frac{55\zeta_3}{36}\right) + C_A N_f\left(-\frac{287}{288} - \frac{5\pi^2}{72} - \frac{2\zeta_3}{9}\right) \\
& + C_F N_f\left(-\frac{41}{48} + \frac{\zeta_3}{2}\right) + \frac{499\zeta_3}{48}
\end{aligned} \tag{3.25}$$

Finally, we conclude this section by reporting two further non-standard settings related to the showering of the $Z\gamma$ MiNNLO$_{PS}$ events. First, we turn on by default the POWHEG-BOX `doublefsr` option, which was introduced and discussed in detail in ref. [114]. When this option is turned on, both $q \to qg$ splittings and $g \to q\bar{q}$ splittings are treated symmetrically for the definition of the starting scale of the shower. This considerably reduces the appearance of spikes in distributions due to events with large weights that pass fiducial cuts after showering, and it ensures a proper treatment of observables sensitive to radiation off such configurations. Furthermore, for the Pythia8 shower [115], we set the flag `SpaceShower:dipoleRecoil 1` (see ref. [116]). Its effect is to have a local recoil scheme (i.e. one that does not affect the colour-singlet system) for initial-final colour dipole emissions, while keeping a global recoil (i.e. one that affects all final state particles including the colour-singlet system) for initial-initial ones. The reason for this choice is that, as shown in ref. [71], a local recoil for initial-final emissions reduces the effect of the shower on the colour-singlet kinematics, in particular in large rapidity regions.

4 Phenomenological results

In this section, we present NNLO+PS accurate predictions for $Z\gamma$ production. We consider different fiducial selections discussing both integrated cross sections and differential distributions in presence of fiducial cuts. MiNNLO$_{PS}$ predictions are compared to NNLO and MiNLO$'$ results. This allows us to validate the accuracy of our predictions for observables

inclusive over QCD radiation and observables requiring the presence of jets. At the same time, we highlight the importance of both NNLO accuracy in the event simulation and the inclusion of parton-shower effects. Finally, we compare MiNNLO$_{\rm PS}$ predictions to a recent ATLAS measurement [1].

4.1 Input parameters, settings and fiducial cuts

We present predictions for 13 TeV collisions at the LHC. Our results have been obtained by using the G_μ-scheme, where the electroweak coupling is defined as

$$\alpha_{G_\mu} = \frac{\sqrt{2} G_\mu m_{\rm W}^2 \sin^2 \theta_{\rm W}}{\pi}, \tag{4.1}$$

where $\cos^2 \theta_{\rm W} = m_{\rm W}^2/m_{\rm Z}^2$ and the input parameters are set to

$$
\begin{aligned}
m_{\rm W} &= 80.385 \text{ GeV}, & m_{\rm Z} &= 91.1876 \text{ GeV}, & G_\mu &= 1.16637 \times 10^{-5} \text{ GeV}^{-2}, \\
\Gamma_{\rm W} &= 2.085 \text{ GeV}, & \Gamma_{\rm Z} &= 2.4952 \text{ GeV}.
\end{aligned} \tag{4.2}
$$

We use $N_{\rm f} = 5$ massless quark flavours, and we choose the corresponding NNLO PDF set of NNPDF3.0 [117] with a strong coupling constant of $\alpha_s(m_{\rm z}) = 0.118$. For the fixed-order predictions we use the PDF set at the respective order in QCD perturbation theory. To be precise, in the case of MiNLO$'$ and MiNNLO$_{\rm PS}$ we read the PDF grids using the LHAPDF interface [118], copy them into HOPPET grids [119] and for scales below the internal PDF infrared cutoff we use HOPPET to consistently perform the DGLAP evolution of the PDFs keeping the number of active flavours fixed to the one at the internal PDF infrared cutoff, as described in ref. [71]. The calculation of $\mathcal{D}_{\ell_{\rm F}}(p_{\rm T})$ in eq. (3.12) requires the evaluation of different PDF convolutions and the computation of polylogarithms. For the latter we made use of the HPLOG package [120].

Our setting of the central renormalization and factorization scales $(\mu_{\rm R,0}, \mu_{\rm F,0})$, which is in line with the MiNNLO$_{\rm PS}$ (MiNLO$'$) method, has been discussed at length in section 3.3, see eqs. (3.17) and (3.19). In all fixed-order results presented throughout this section we adopt the following setting of the central renormalization and factorization scales:

$$\mu_{\rm R,0} = \mu_{\rm F,0} = m_{\ell\ell\gamma}, \tag{4.3}$$

where $m_{\ell\ell\gamma}$ is the invariant mass of the $Z\gamma$ system. The different scale choice between a NLO/NNLO fixed-order and a MiNLO$'$/MiNNLO$_{\rm PS}$ calculation induces effects beyond the nominal accuracy, in addition to the different treatment of higher-order terms, see comments close to eq. (3.12). As a results, minor differences between the fixed-order and matched predictions are expected even for more inclusive observables. Nevertheless, the results should largely agree within scale uncertainties, at least in cases where scale uncertainties are expected to be a reliable estimate of missing higher-order corrections.

We employ 7-point scale variations as an estimate of the theoretical uncertainties. Accordingly, the minimum and maximum of the cross section have been taken over a set of scales $(\mu_{\rm R}, \mu_{\rm F})$ obtained by varying $K_{\rm R}$ and $K_{\rm F}$ in $\mu_{\rm R} = K_{\rm R} \mu_{\rm R,0}$ and $\mu_{\rm F} = K_{\rm F} \mu_{\rm F,0}$, respectively, within the values

$$(K_{\rm R}, K_{\rm F}) = \{(2,2), (2,1), (1,2), (1,1), (1,1/2), (1/2,1), (1/2,1/2)\}. \tag{4.4}$$

We reiterate that, when performing scale variations for MiNLO′ and MiNNLO$_{\rm PS}$, we also include the scale dependence of the Sudakov form factor to account for additional sources of uncertainties [70], which are absent in a fixed-order calculation.

For all technical details and choices made for our implementation of the $Z\gamma$+jet generator as well as for the treatment of the NNLO corrections through the MiNNLO$_{\rm PS}$ method we refer the reader to section 2.3 and section 3.3, respectively. In particular, the settings discussed in section 2.3 are essential to get a good convergence of the Monte Carlo integration and an efficient event generation, by adopting generation cuts and individual suppression factors at Born level, for the singular real contributions and the remnant contributions (cf. also appendix A). In addition, folding of the radiation variables (ξ, y, ϕ) [87, 97] has been used, with a choice of $(1, 5, 1)$ for the folding parameters, to evaluate the double-real correction ($Z\gamma$+2-jet) more often, which further improves the numerical convergence. Despite all those efforts to achieve a better numerical performance, we had to produce ~ 100 million $Z\gamma$ events with our MiNNLO$_{\rm PS}$ generator to obtain acceptable statistical uncertainties and predict integrated cross sections in the fiducial setups considered here at the level of a few permille. Still, our comparison of differential distributions to NNLO predictions suffers from some fluctuations. We note, however, that with $Z\gamma$ production we have picked probably the most involved diboson process, featuring various complications, in particular considering its substantial complexity with respect to the QED singularity structure. We therefore expect other diboson processes to have a much lower demand for numerical resources.

As pointed out before, we omit the loop-induced gluon fusion process in our implementation and throughout this paper. This contribution is relatively small, being only $\sim 1\%$ of the NNLO cross section, and it can be incoherently added to our predictions through a dedicated calculation, which, however, is beyond the scope of this paper. Consequently, we drop the loop-induced gluon fusion contribution also from the fixed-order calculation, when comparing MiNNLO$_{\rm PS}$ against NNLO results, to warrant a meaningful comparison.

We employ the Pythia8 parton shower [115] with one of the A14 tunes [121] (specifically py8tune 21) to dress the hard event with further soft/collinear QCD radiation and use the default POWHEG setting for the parton-shower starting scale. Hadronization effects are studied in section 4.5 when comparing against data. Otherwise, the showered results do not include any effects from hadronization or underlying event models. Moreover, the photon is required to be generated only at the hard scattering level: contributions from a QED shower or the decay of unstable particles is not included. Finally, we keep photons stable by preventing any photon conversion effect, i.e. no $\gamma \to \ell^+\ell^-$ or $\gamma \to \bar{q}q$ splittings.

We present results for two sets of fiducial cuts, which are summarized in table 1. The first one is identical to that used in refs. [22, 85] and motivated by in an earlier ATLAS analysis [43]. We refer to it as ATLAS-setup-1 in the following. The second one was instead used in the most recent ATLAS 13 TeV measurement of ref. [1] using the full Run-2 data and named ATLAS-setup-2 in the following. We make use of ATLAS-setup-1 only for validation purposes and to show the importance of NNLO+PS matching, while ATLAS-setup-2 is also used to compare MiNNLO$_{\rm PS}$ predictions with the most updated experimental measurement available for $Z\gamma$ production. Both setups in table 1 involve stan-

	ATLAS-setup-1 [43]	ATLAS-setup-2 [1]
Lepton cuts	$p_{\mathrm{T},\ell} > 25\,\mathrm{GeV}$ $\lvert\eta_\ell\rvert < 2.47$	$p_{\mathrm{T},\ell_1} > 30\,\mathrm{GeV}$ $p_{\mathrm{T},\ell_2} > 25\,\mathrm{GeV}$
	$m_{\ell\ell} > 40\,\mathrm{GeV}$	$\lvert\eta_\ell\rvert < 2.47$ $m_{\ell\ell} > 40\,\mathrm{GeV}$
	–	$m_{\ell\ell} + m_{\ell\ell\gamma} > 182\,\mathrm{GeV}$
Photon cut	$p_{\mathrm{T},\gamma} > 15\,\mathrm{GeV}$ $\lvert\eta_\gamma\rvert < 2.37$	$p_{\mathrm{T},\gamma} > 30\,\mathrm{GeV}$ $\lvert\eta_\gamma\rvert < 2.37$
Separation cuts	$\Delta R_{\ell\gamma} > 0.7$	$\Delta R_{\ell\gamma} > 0.4$
	$\Delta R_{\ell,j} > 0.3$ $\Delta R_{\gamma j} > 0.3$	—
Jet definition	anti-k_{T} algorithm with $R = 0.4$	–
	$p_{\mathrm{T},j} > 30\,\mathrm{GeV}$ $\lvert\eta_j\rvert < 4.4$	—
Photon Isolation	Frixione isolation with	Frixione isolation with
	$n = 1$ $\epsilon_\gamma = 0.5$ $\delta_0 = 0.4$	$n = 2$ $\epsilon_\gamma = 0.1$ $\delta_0 = 0.1$
		$+$ $E_{\mathrm{T}}^{\mathrm{cone}0.2}/p_{\mathrm{T},\gamma} < 0.07$

Table 1. Fiducial cuts in two different ATLAS setups denoted as `ATLAS-setup-1` and `ATLAS--setup-2`. See text for details.

dard transverse-momentum and pseudorapidity thresholds to identify leptons and photons, as well as a lower invariant-mass cut on the lepton pair. `ATLAS-setup-2` places an additional requirement on the sum of the invariant masses of the $Z\gamma$ system and of the lepton pair. This cut suppresses the contribution from ℓ-type diagrams, where the photon is emitted from the final state leptons (cf. figure 1b), enhancing t-channel production through q-type diagrams (cf. figure 1a). Moreover, separation cuts between two particles (i, j) are applied in $\Delta R_{ij} = \sqrt{\Delta\eta_{ij}^2 + \Delta\phi_{ij}^2}$, where $\Delta\eta_{ij}$ and $\Delta\phi_{ij}$ are their differences in the pseudorapidity and the azimuthal angle, respectively. In both setups leptons are separated from the isolated photon, while only `ATLAS-setup-1` imposes an additional separation of jets from leptons and from the isolated photon, which in turn requires a jet definition.[9] As a consequence, we employ `ATLAS-setup-1` to study jet observables and show NLO/LO accuracy of MiNNLO$_{\mathrm{PS}}$ predictions for $Z\gamma$+jet/$Z\gamma$+2-jet configurations. Finally, isolation criteria for the photon are needed, as detailed in section 2.3, which is done by means of Frixione isolation in both setups. In `ATLAS-setup-2`, Frixione isolation is applied within a smaller cone and a second isolation criterium is added by requiring the scalar sum of the transverse energy of all stable particles (except neutrinos and muons) within a cone around the photon of size $R = 0.2$ ($E_{\mathrm{T}}^{\mathrm{cone}0.2}$) to be less than 7% of the photon transverse momentum (see ref. [1] for more details). Note that we apply the latter isolation criterium only when analyzing events after parton showering, but not at Les-Houches-Event (LHE) or fixed-order level.

4.2   Fiducial cross sections

In table 2 we report predictions for the $Z\gamma$ cross section in the two fiducial setups at LO, NLO and NNLO, and for MiNLO′ and MiNNLO$_{\mathrm{PS}}$ matched to Pythia8. The fixed-order results have been obtained with Matrix [85, 106]. Although MiNNLO$_{\mathrm{PS}}$ and

---

[9]We stress that `ATLAS-setup-1` is inclusive over jets and that jet-separation cuts are only applied when a jet is present.

	ATLAS-setup-1 [43]		ATLAS-setup-2 [1]	
	$\sigma_{\text{inclusive}}$ [pb]	$\sigma/\sigma_{\text{NNLO}}$	$\sigma_{\text{inclusive}}$ [fb]	$\sigma/\sigma_{\text{NNLO}}$
LO	$1.5032(1)^{+11.2\%}_{-11.9\%}$	0.656	$271.83(2)^{+6.8\%}_{-7.8\%}$	0.508
NLO	$2.1170(5)^{+2.8\%}_{-4.3\%}$	0.924	$456.6(1)^{+3.6\%}_{-3.0\%}$	0.853
NNLO	$2.290(3)^{+0.9\%}_{-1.0\%}$	1.000	$535.3(6)^{+2.7\%}_{-2.5\%}$	1.000
MiNLO'	$2.222(8)^{+8.8\%}_{-11.0\%}$	0.970	$516(4)^{+8.8\%}_{-6.5\%}$	0.964
MiNNLO$_{\text{PS}}$	$2.299(5)^{+1.6\%}_{-1.4\%}$	1.004	$529(2)^{+4.0\%}_{-3.2\%}$	0.988
ATLAS	—		$533.7 \pm 2.1_{\text{(stat)}} \pm 12.4_{\text{(syst)}} \pm 9.1_{\text{(lumi)}}$	

Table 2. Predictions for fiducial cross sections of $Z\gamma$ production at LO, NLO, and NNLO, as well as using the MiNLO' and MiNNLO$_{\text{PS}}$ calculations, in the two ATLAS setups. For comparison, a column with the ratio to the NNLO cross section is shown. In the last row the ATLAS measurement of ref. [1] is reported.

NNLO calculations entail a different treatment of terms beyond accuracy, in both setups the agreement of their predicted cross sections is remarkably good. One should bear in mind, however, that in `ATLAS-setup-2` there is a slight difference in the treatment of the isolated photon at fixed order, which does not include the $E_{\text{T}}^{\text{cone0.2}}/p_{\text{T},\gamma} < 0.07$ cut, as discussed in the previous section. We further notice from table 2 that the scale uncertainties of the NNLO and MiNNLO$_{\text{PS}}$ predictions are larger in `ATLAS-setup-2`. This is caused by the additional $m_{\ell\ell} + m_{\ell\ell\gamma}$ cut and the stronger cut on the photon transverse momentum in that fiducial setup, rendering the predictions more sensitive to additional QCD radiation that is described at a lower perturbative accuracy.

Comparing MiNNLO$_{\text{PS}}$ and MiNLO' predictions, the inclusion of NNLO corrections through MiNNLO$_{\text{PS}}$ has a relatively moderate effect for the fiducial cross section of $+3.5\%$ in `ATLAS-setup-1` and $+2.5\%$ in `ATLAS-setup-2`. In fact, in both cases (and particularly evident for the latter setup) MiNLO' predictions are actually closer to the NNLO results than to the NLO ones. After all, the Sudakov form factor in eq. (3.5) is exactly the same for MiNNLO$_{\text{PS}}$ and MiNLO', and MiNLO' predictions already contain various contributions beyond NLO accuracy, including all real corrections at NNLO through the merging of NLO corrections to $Z\gamma$+jet production. Still, by reaching NNLO accuracy through the MiNNLO$_{\text{PS}}$ procedure the predictions get even closer to the NNLO results and the uncertainty bands substantially decrease, by almost a factor of ten in `ATLAS-setup-1` and by more than a factor of two in `ATLAS-setup-2`. Indeed, the MiNNLO$_{\text{PS}}$ scale uncertainties are comparable with the NNLO ones. The fact that they are slightly larger is expected since the MiNNLO$_{\text{PS}}$ procedure probes lower scales both in the PDFs and in α_s, and it includes scale variations also for the Sudakov form factor.

Finally, we find excellent agreement of our NNLO+PS accurate MiNNLO$_{\text{PS}}$ predictions with the cross section measured by ATLAS in ref. [1], which are perfectly compatible within the quoted experimental errors.
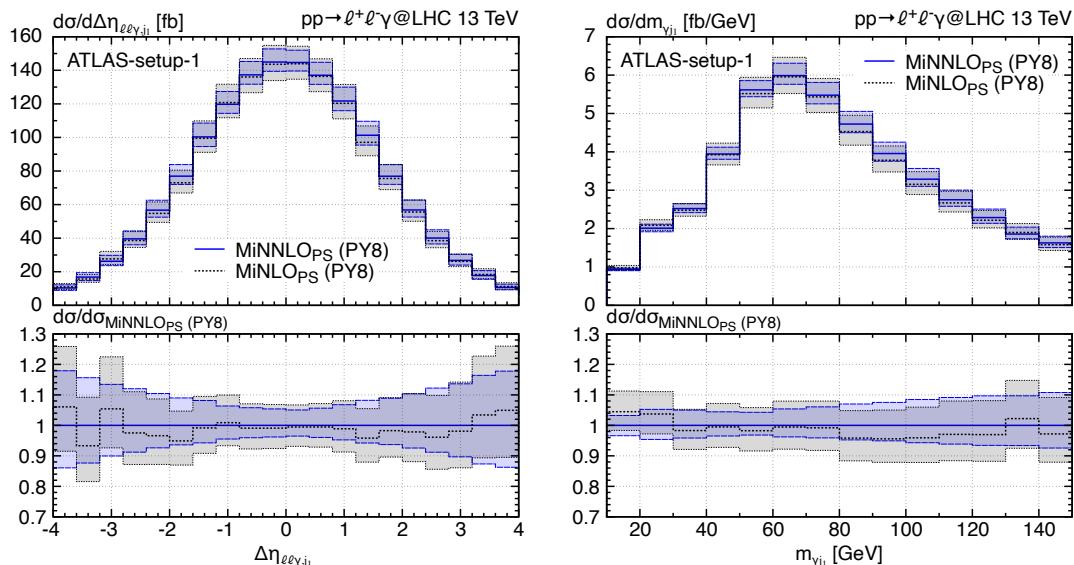
Figure 4. Distribution in the pseudorapidity difference of the colour-singlet and the hardest jet (left plot) and in the invariant mass of the photon and the hardest jet (right plot) for MiNNLO$_{PS}$ (blue, solid line) and MiNLO' (black, dotted line).
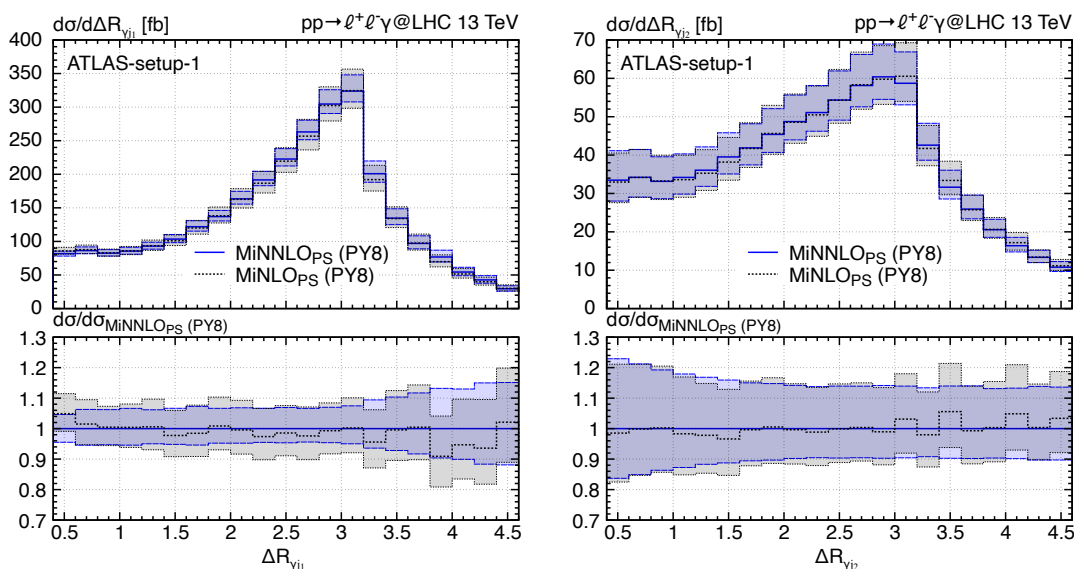

Figure 5. Distribution in the ΔR separation between the photon and hardest jet (left plot), and between the photon and the second-hardest jet (right plot) for MiNNLO$_{PS}$ (blue, solid line) and MiNLO' (black, dotted line).

4.3 Comparison of differential distributions against MiNLO' and NNLO

We now turn to discussing differential distributions in the fiducial phase space. In this section we compare our MiNNLO$_{PS}$ predictions with MiNLO' and NNLO results. This serves two purposes. On the one hand, MiNNLO$_{PS}$ distributions are validated for one-jet and two-jet observables against the ones obtained with MiNLO' and for Born-level

observables (inclusive over QCD radiation) against NNLO predictions. On the other hand, this allows us to show the importance of NNLO+PS matching with respect to less accurate results. To these ends, we discuss selected distributions which are particularly significant to show the performance of MiNNLO$_{PS}$ predictions. The figures of this and the upcoming sections are organized as follows: the main frame shows the predictions from MiNNLO$_{PS}$ matched to Pythia8 (blue, solid line), together with all other results relevant for the given comparison. In an inset we display the bin-by-bin ratio of all the histograms that appear in the main frame to the MiNNLO$_{PS}$ one. The bands indicate the theoretical uncertainties that are computed from scale variations.

We start by discussing quantities that involve jets in the final state in figure 4 and figure 5, where MiNNLO$_{PS}$ (blue, solid line) and MiNLO′ (black, dotted line) matched to Pythia8 are compared in `ATLAS-setup-1`. Since for these observables MiNLO′ and MiNNLO$_{PS}$ have the same accuracy the two predictions are expected not to differ from each other significantly (i.e. not beyond uncertainties), both in terms of shapes and size of scale uncertainty bands. In particular, such agreement serves as a validation that NNLO corrections are properly spread by the factor in eq. (3.14) in the jet-resolved phase space of $Z\gamma$+jet production without altering the NLO accuracy. As a matter of fact, the left plot of figure 4 shows that MiNNLO$_{PS}$ and MiNLO′ predictions agree well within uncertainties for the pseudorapidity difference between the $Z\gamma$ system and the hardest jet ($\Delta\eta_{\ell\ell\gamma,\,j_1}$). Furthermore, the size of the uncertainty bands are comparable over the whole pseudorapidity range. In a similar manner, the ratio between MiNNLO$_{PS}$ and MiNLO′ is nearly flat for the invariant mass of the photon and the hardest jet ($m_{\gamma j_1}$) in the right plot of figure 4. Here, we further observe the effect of the Frixione isolation, which dampens the distribution in the photon-jet collinear limit. Also in figure 5 MiNNLO$_{PS}$ and MiNLO′ predictions agree well for the distance between the photon and the leading and subleading jet in the η-ϕ plane ($\Delta R_{\gamma j_1}$ and $\Delta R_{\gamma j_2}$). As $\Delta R_{\gamma j_2}$ involves the second-hardest jet, both MiNNLO$_{PS}$ and MiNLO′ are only LO accurate, which is also evident from the broadening of the uncertainty bands. We have examined a large number of other quantities involving jets (not shown here) observing a similar behaviour in all cases.

Next, in figure 6, figure 7 and figure 8, we compare MiNNLO$_{PS}$ (blue, solid line) against MiNLO′ (black, dotted line) and NNLO predictions from Matrix [85, 106] (red, dashed line) for Born-level observables (inclusive over QCD radiation). By and large, we observe a very good agreement of MiNNLO$_{PS}$ and NNLO predictions, especially considering the fact that they differ from each other in the choice of the renormalization and factorization scales, and in the treatment of higher-order contributions. What can be appreciated is the clear reduction of the scale uncertainties of MiNNLO$_{PS}$ predictions with respect to the MiNLO′ ones up to a size which is comparable to the NNLO ones.

In particular, figure 6 displays the pseudorapidity distribution of the $Z\gamma$ system ($\eta_{\ell\ell\gamma}$) in each of the two fiducial setups. The ratio of NNLO over MiNNLO$_{PS}$ is close to one in both cases, with uncertainty bands of one to two percent in `ATLAS-setup-1`. In `ATLAS-setup-2`, on the other hand, the bands are roughly twice as large, as already observed for the integrated cross section due to the higher sensitivity to phase-space regions related to real QCD radiation.
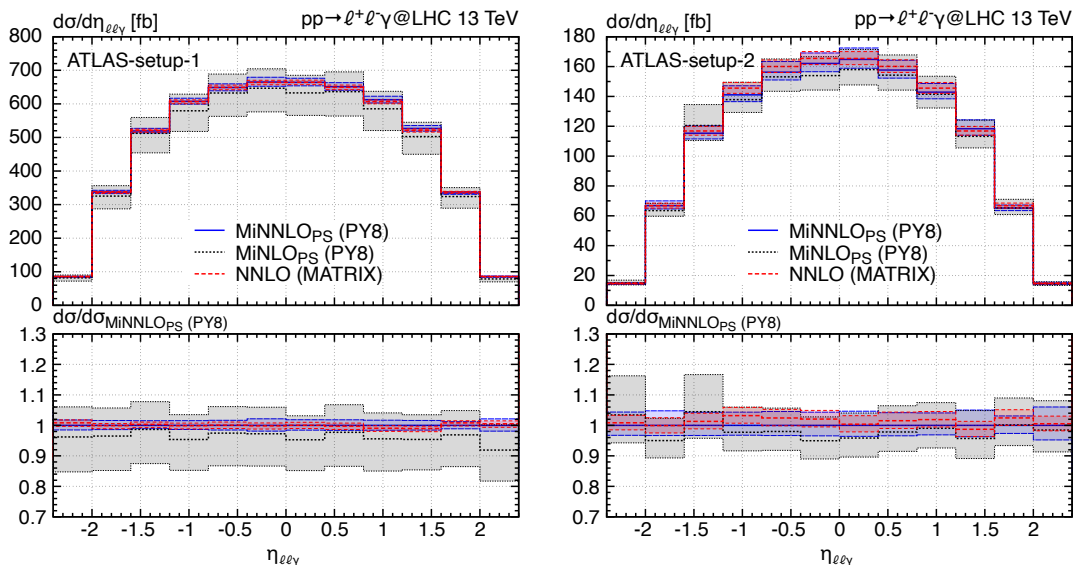
Figure 6. Distribution in the pseudorapidity of the $Z\gamma$ system in `ATLAS-setup-1` (left plot) and in `ATLAS-setup-2` (right plot) for MiNNLO$_{PS}$ (blue, solid line), MiNLO$'$ (black, dotted line) and NNLO (red, dashed line).
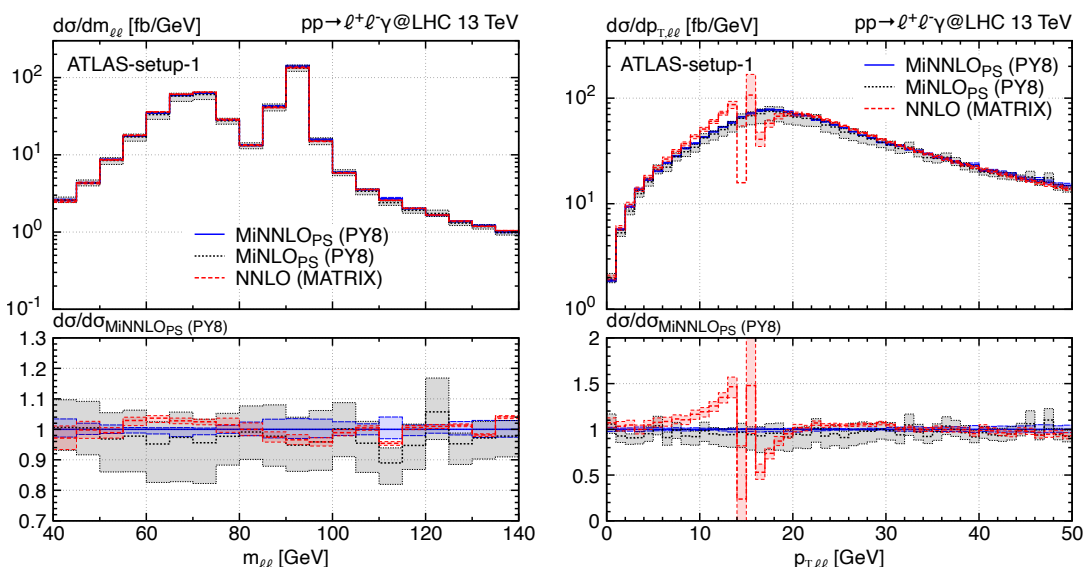

Figure 7. Distribution in the invariant mass (left plot) and in the transverse momentum (right plot) of the lepton pair for MiNNLO$_{PS}$ (blue, solid line), MiNLO$'$ (black, dotted line) and NNLO (red, dashed line).

In figure 7 we show the distributions in the invariant mass ($m_{\ell\ell}$) and transverse momentum ($p_{T,\ell\ell}$) of the lepton pair in `ATLAS-setup-1`. The qualitative behaviour of MiNNLO$_{PS}$ with respect to MiNLO$'$ and NNLO predictions in the ratio inset is relatively similar to the one of the $Z\gamma$ rapidity distribution. We can appreciate the Z-boson resonance in the $m_{\ell\ell}$ distribution as well as a broader, but smaller, enhancement around $m_{\ell\ell} \sim 70\,\text{GeV}$, caused by the Z-boson resonance in $m_{\ell\ell\gamma}$. Close to the latter resonance, we observe that
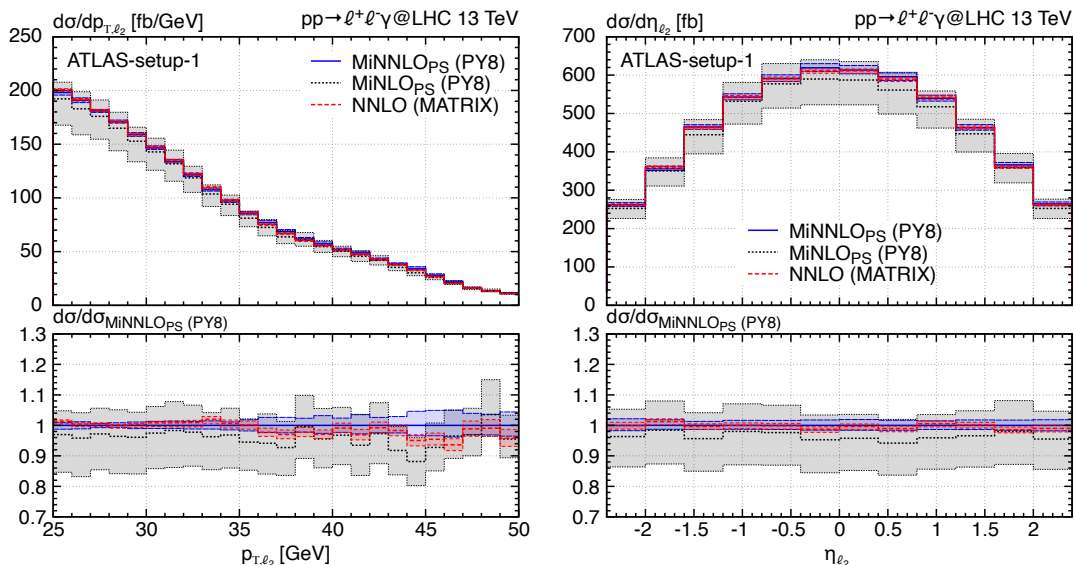
Figure 8. Distribution in the transverse momentum (left plot) and in the pseudorapidity (right plot) of the second-hardest lepton for MiNNLO$_{PS}$ (blue, solid line), MiNLO′ (black, dotted line) and NNLO (red, dashed line).

the MiNNLO$_{PS}$ prediction is $\sim 4\%$ below the NNLO prediction, without overlapping uncertainty bands. The same effect is present at the resonance of the $m_{\ell\ell\gamma}$ spectrum. We have checked that in this region of phase space the $Z\gamma$ system tends to be softer. Therefore, all-order terms related to $p_{T,\ell\ell\gamma}$ have a larger impact. In the $p_{T,\ell\ell}$ distribution we observe an interesting behaviour of the NNLO prediction. The NNLO result develops a perturbative instability (Sudakov shoulder) [122] around $p_{T,\ell\ell} \sim 15\,\mathrm{GeV}$ caused by an incomplete cancellation of virtual and real contributions from soft-gluon emissions, which is logarithmically divergent, but integrable. The reason is the fiducial cut $p_{T,\gamma} > 15\,\mathrm{GeV}$ (see table 1) that for LO kinematics implies $p_{T,\ell\ell} = p_{T,\gamma} > 15\,\mathrm{GeV}$, so that the $p_{T,\ell\ell}$ distribution is not filled below 15 GeV at LO. Thus, the fixed-order result is NNLO accurate only for $p_{T,\ell\ell} > 15\,\mathrm{GeV}$, while for $p_{T,\ell\ell} < 15\,\mathrm{GeV}$ at least one QCD emission is necessary, which is described only at NLO accuracy. At the same time, the prediction becomes sensitive to soft-gluon effects at threshold, resulting in an instability at fixed order. Indeed, the parton shower cures this behaviour and yields a physical prediction at threshold for both MiNLO′ and MiNNLO$_{PS}$. This is one example where a NNLO calculation is insufficient and NNLO+PS matching is required.

In figure 8 we consider distributions in the second-hardest lepton, showing its transverse momentum (p_{T,ℓ_2}) in the left and its rapidity (η_{ℓ_2}) in the right plot. Similar conclusions as made before for $m_{\ell\ell}$ and $\eta_{\ell\ell\gamma}$ apply also for these observables, so no further comments are needed. We reiterate however that, while the central predictions of MiNLO′ and MiNNLO$_{PS}$ are generally close to each other, since MiNLO′ already includes many terms beyond NLO accuracy for $Z\gamma$ production, scale uncertainties are substantially reduced in case of MiNNLO$_{PS}$, down to the level of the NNLO ones.
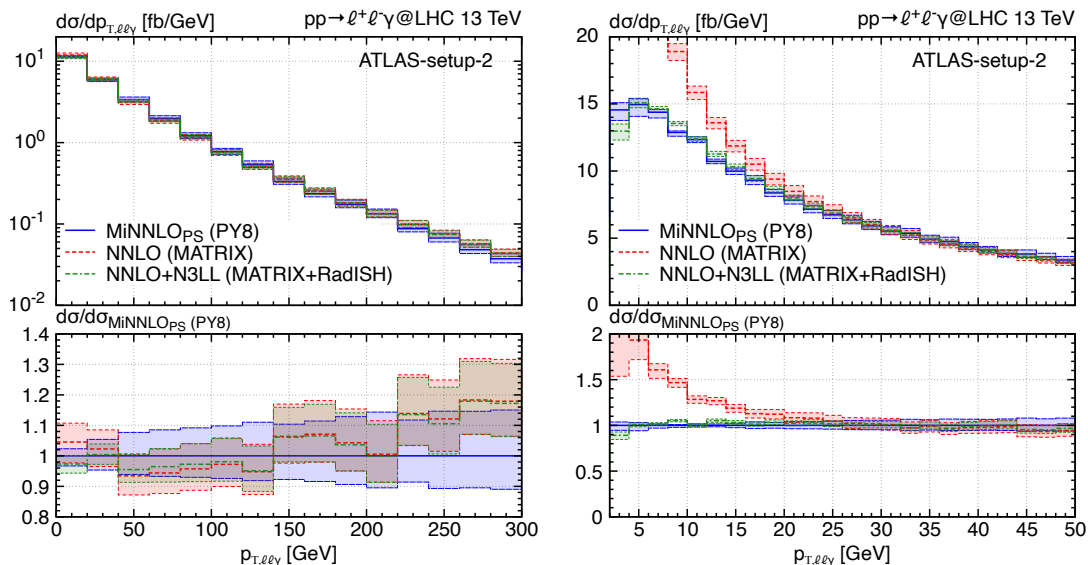
Figure 9. Distribution in the transverse momentum of the $Z\gamma$ system in a wider range (left plot) and at small $p_{\mathrm{T},\ell\ell\gamma}$ (right plot) for MiNNLO$_{\mathrm{PS}}$ (blue, solid line), NNLO (red, dashed line) and NNLO+N^{3}LL (green, double-dash-dotted line).

4.4 Comparison of $Z\gamma$ transverse-momentum spectrum against NNLO+N^{3}LL

We continue our discussion of differential distributions with the transverse-momentum spectrum of the $Z\gamma$ system ($p_{\mathrm{T},\ell\ell\gamma}$). In figure 9 we compare the $p_{\mathrm{T},\ell\ell\gamma}$ distribution in `ATLAS-setup-2` obtained with MiNNLO$_{\mathrm{PS}}$ against a more accurate prediction at NNLO+N^{3}LL (green, double-dash-dotted line), using the analytic resummation of large logarithmic contributions within MATRIX+RADISH [59, 61]. For comparison we also show the NNLO result, which is effectively only NLO accurate for this distribution. Bear in mind that those two predictions include the full heavy-quark mass dependence, which has an impact at large values of $p_{\mathrm{T},\ell\ell\gamma}$, see appendix C. The NNLO+N^{3}LL prediction uses [59]

$$\mu_{\mathrm{R},0} = \mu_{\mathrm{F},0} = \sqrt{m_{\ell\ell}^2 + p_{\mathrm{T},\gamma}^2} \quad \text{and} \quad Q_{\mathrm{res},0} = \frac{1}{2} m_{\ell\ell\gamma} \tag{4.5}$$

as central scales, where $Q_{\mathrm{res},0}$ is the central resummation scale. $Q_{\mathrm{res},0}$ is varied by a factor of two up and down, while taking the envelope together with the 7-point μ_{R} and μ_{F} variation for the total scale uncertainty.

The $p_{\mathrm{T},\ell\ell\gamma}$ spectrum is shown in two different ranges in figure 9. From the wider range in the left plot we notice that despite the different scale settings in the three calculations their predictions are in reasonable agreement at large $p_{\mathrm{T},\ell\ell\gamma}$ values. The fact that for $p_{\mathrm{T},\ell\ell\gamma} \gtrsim 150\,\mathrm{GeV}$ the NNLO and NNLO+N^{3}LL predictions become successively harder than the MiNNLO$_{\mathrm{PS}}$ one is related to the heavy-quark mass effects, see appendix C. At large $p_{\mathrm{T},\ell\ell\gamma}$ all predictions are effectively NLO accurate, which is indicated by the enlarged scale-uncertainty bands. At small $p_{\mathrm{T},\ell\ell\gamma}$ the fixed-order result becomes unphysical, as the distribution is logarithmically divergent in the $p_{\mathrm{T}} \to 0$ limit, which is visible already in the left plot of figure 9, but can be better appreciated in the zoomed version on the right.

In this region, only the calculations that properly account for the resummation of soft QCD radiation by means of an analytic procedure (NNLO+N³LL) or through parton-shower simulations (MiNNLO$_{PS}$) provide a meaningful description. Even though at small $p_{T,\ell\ell\gamma}$ the Matrix+Radish computation is N³LL accurate, while the parton shower has a lower logarithmic accuracy, MiNNLO$_{PS}$ and NNLO+N³LL predictions are in excellent agreement down to transverse-momentum values (almost) in the non-perturbative regime.

4.5 Comparison of differential distributions against ATLAS data

Finally, we employ our MiNNLO$_{PS}$ generator to compare NNLO+PS accurate predictions directly to ATLAS results from the recent 13 TeV measurement of ref. [1], which relies on the full 139 fb^{-1} Run-2 data. The comparison, carried out in `ATLAS-setup-2`, is presented in figure 10. The experimental data are given as green points with error bars that refer to the experimental uncertainty. Six observables are shown: the transverse momentum ($p_{T,\gamma}$) and the pseudorapidity (η_γ) of the photon, the transverse momentum ($p_{T,\ell\ell\gamma}$) and the invariant mass ($m_{\ell\ell\gamma}$) of the $Z\gamma$ system, together with their ratio $p_{T,\ell\ell\gamma}/m_{\ell\ell\gamma}$ and the difference in the azimuthal angle between the lepton pair and the photon ($\Delta\phi_{\ell\ell,\gamma}$).

To assess effects from hadronization, in addition to our partonic MiNNLO$_{PS}$ result (blue, solid) we also show a curve where the hadronization of the partonic events is modelled through Pythia8 (magenta, dash-dotted). The hadronic final states are kept stable and multi-parton interactions are turned off to avoid secondary photons and maintain a sufficiently simple analysis. By and large, we find minor contributions from hadronization for the observables considered here. They are at the level of the statistical uncertainties and well within scale variations.

Overall, we observe a remarkably good agreement with data both in the predicted shapes of the distributions and in the normalization, especially given the fact that the theoretical and the experimental uncertainties are at the few-percent level only. All data points agree with our predictions within the experimental error bars, with the exception of only very few bins, where the agreement is reached within twice the experimental error. This is a clear improvement over the NLO-accurate event simulations employed in the data-theory comparison in figure 6 of ref. [1], both in terms of accuracy (i.e. to describe the data) and in terms of precision (i.e. regarding theoretical uncertainties). Moreover, looking at the comparison of NNLO predictions to data in figure 7 of ref. [1], it is clear that some (more inclusive) observables are equally well described at fixed order, while for observables sensitive to QCD radiation, such as $p_{T,\ell\ell\gamma}$ and $\Delta\phi_{\ell\ell,\gamma}$, NNLO predictions are not sufficient, and the matching to a parton shower is essential. In conclusion, our MiNNLO$_{PS}$ calculation combines the two most important aspects (NNLO and parton-shower effects) to provide the most accurate and most precise $Z\gamma$ predictions to date, which will be essential to find potential deviations from the SM for this process in future.

Let us discuss in more detail the $p_{T,\ell\ell\gamma}$ distribution in figure 10. In this plot we have also added the more accurate NNLO+N³LL prediction, as introduced in section 4.4 with the scale setting of eq. (4.5) and including heavy-quark mass effects. We recall that the latter induce differences at large $p_{T,\ell\ell\gamma}$, see appendix C, which are visible in the last bin. Despite the good agreement of MiNNLO$_{PS}$ with data, the analytically resummed result
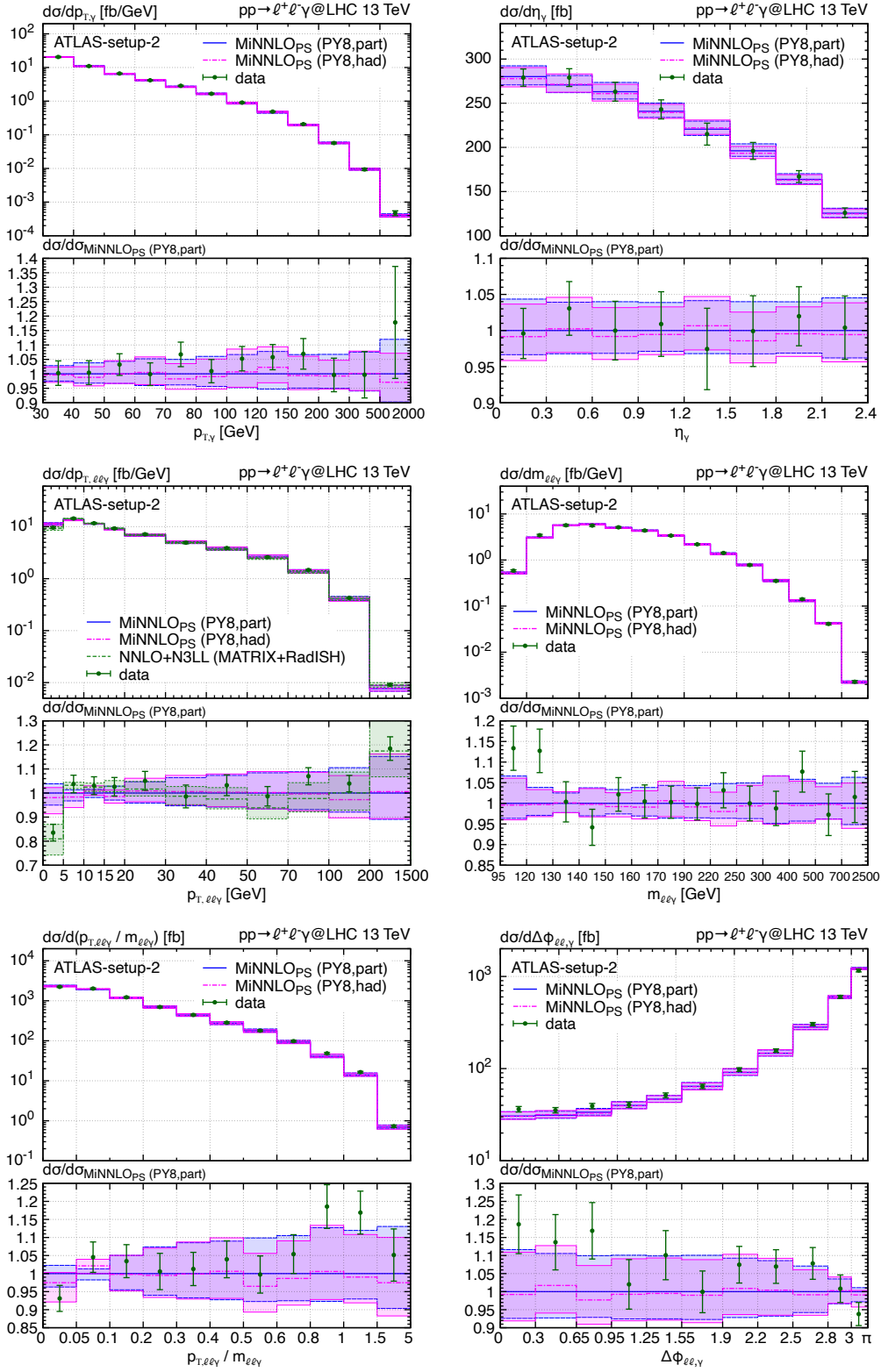
Figure 10. MiNNLO_PS predictions at parton level (blue, solid line) and including hadronization (magenta, dash-dotted) compared to ATLAS 13 TeV data (green points with error bars). For $p_{\mathrm{T},\ell\ell\gamma}$ also NNLO+N³LL (green, double-dash-dotted line) is shown.

is performing even better, especially in the first few bins, where the higher accuracy in the resummation of large logarithmic contributions is important. Although MiNNLO$_{\rm PS}$ and NNLO+N^{3}LL agree quite well (cf. the discussion in section 4.4), this shows that for an observable like $p_{\rm T,\ell\ell\gamma}$ it can be very useful to resort to tools that predict a single distribution more accurately, if available. Nevertheless, it is reassuring that our accurate multi-purpose MiNNLO$_{\rm PS}$ simulation, with all its flexibility to predict essentially any IR-safe observable, provides a very good description of such distributions as well.

We further notice that the deviation at small $m_{\ell\ell\gamma}$ is due to missing QED effects as shown in ref. [1]. Our MiNNLO$_{\rm PS}$ computation renders the inclusion of such effects into NNLO-accurate predictions feasible by using a QED shower within Pythia8, which could be very useful in an experimental analysis. This is however beyond the scope of this paper and left for future studies.

5 Summary

We have presented a novel calculation of NNLO+PS accurate predictions to $Z\gamma$ production at the LHC. This is the first calculation of a genuine $2 \to 2$ process at this accuracy that does not require an a-posteriori multi-differential reweighting. To this end, we have extended the MiNNLO$_{\rm PS}$ method [70] to $2 \to 2$ colour-singlet production, with non-trivial one-loop and two-loop corrections, and applied it to the $Z\gamma$ process. More precisely, we have considered all resonant and non-resonant contributions to the hard-scattering process $pp \to \ell^+\ell^-\gamma$, including off-shell effects and spin correlations.

As a starting point we have implemented NLO+PS generators for both $Z\gamma$ and $Z\gamma$+jet production within the POWHEG-BOX-RES framework [88]. The $Z\gamma$+jet generator has then been extended to include NNLO corrections to $Z\gamma$ production by means of the MiNNLO$_{\rm PS}$ method. The two-loop virtual corrections [105] are linked through their implementation within the Matrix code [85], which we treat as a library. A substantial amount of work has been devoted to render those calculations numerically efficient, and we have discussed the technical and physical aspects in detail. All our computations will be made publicly available within POWHEG-BOX-RES.[10]

We have presented NNLO+PS accurate predictions using our MiNNLO$_{\rm PS}$ calculation in proton-proton collisions at 13 TeV. Observables exclusive in the final state jets have been used to validate the way we include NNLO corrections through the MiNNLO$_{\rm PS}$ procedure by comparing MiNNLO$_{\rm PS}$ with MiNLO$'$ predictions. Observables inclusive over QCD radiation are generally well described by a fixed-order NNLO calculation. Although MiNNLO$_{\rm PS}$ predictions differ in the treatment of terms beyond accuracy, we found them to be in very good agreement with NNLO results, both for fiducial cross sections and for differential distributions. Moreover, we have shown the importance of NNLO+PS accurate predictions. On the one hand, they render predictions physical for observables sensitive to soft-gluon effects, where NNLO results fail to provide a suitable description. On the other hand, the inclusion of NNLO corrections through MiNNLO$_{\rm PS}$ achieves a

---

[10]Instructions to download the $Z\gamma$ and $Z\gamma$+jet generators (including the MiNNLO$_{\rm PS}$ features) will be provided on http://powhegbox.mib.infn.it and those generators are already available upon request.

substantial improvement over MiNLO′ results in terms of scale uncertainties for inclusive observables. We also compared MiNNLO$_{\text{PS}}$ predictions for the $Z\gamma$ transverse-momentum spectrum against a more accurate analytically resummed calculation at NNLO+N^{3}LL and found a remarkable agreement down to transverse-momentum values close to the non-perturbative regime. Finally, we have shown that MiNNLO$_{\text{PS}}$ predictions are in excellent agreement with the latest ATLAS 13 TeV data, featuring various improvements over lower-order simulations.

This calculation paves the way for NNLO+PS predictions for all diboson processes in the future. Moreover, the contribution from the loop-induced gluon fusion process, despite being rather small for $Z\gamma$ production, could be calculated separately at (N)LO+PS and added to our predictions. A rather straightforward advancement would also be to consider $Z \to \nu\bar{\nu}$ decays in future, which will be highly relevant also for dark-matter searches. In this context, also suitable modifications of the SM could be considered, for instance by introducing effective $Z^\star Z\gamma$ and $\gamma^\star\gamma Z$ couplings.

Finally, we reckon that the presented results as well as our MiNNLO$_{\text{PS}}$ generator for $Z\gamma$ production will be a useful advancement over previous Monte Carlo predictions and tools. Especially since the MiNNLO$_{\text{PS}}$ generator can be directly applied in experimental analyses for $Z\gamma$ measurements and searches, the improved theoretical predictions in terms of accuracy and precision might stimulate further studies of this process in future.

Note added. On the same day the present article appeared on arXiv.org, the matching of NNLO corrections with parton showers for another genuine $2 \to 2$ process, namely $\gamma\gamma$ production, was posted [123].

A Generation cuts and suppression factors

Since our Born process involves a number of QED and QCD singularities, we make use of Born and remnant suppression factors to sample the phase space. Additionally, we introduce a number of small technical cuts in the phase-space generation. In this appendix we give all details about the generation cuts and suppression factors that we have used to obtain the results presented in this paper.

We start by outlining the generation cuts that we employ. First, we introduce a lower cut $p_{\text{T},\gamma}^{\text{cut}} = 5\,\text{GeV}$ on the photon transverse momentum, which is required to avoid QED singularities related to collinear photon emissions from the initial state. We also impose a similar cut of $p_{\text{T},j}^{\text{cut}} = 1\,\text{GeV}$ on the transverse momentum of the outgoing QCD partons.

A lower cut $m_{\ell\ell}^{\text{cut}} = 40\,\text{GeV}$ on the invariant mass of the lepton pair is imposed to avoid singular configurations in $\gamma^* \to \ell^+ \ell^-$ splittings. Note that, since the invariant mass of the resonances are preserved when radiation is generated (both within POWHEG and the shower), any value $m_{\ell\ell}^{\text{cut}}$ equal or below the cut used in the analysis is allowed. Furthermore, we require that the photon is isolated from leptons and QCD partons in the final state. For this purpose, we introduce a cut $m_{\ell\gamma}^2 = 0.1\,\text{GeV}^2$, and we introduce a smooth isolation as in eq. (2.8) with $E_{\text{T}}^{\text{ref}} = \epsilon_\gamma p_{\text{T},\gamma}$ with $\delta_0 = 0.05$, $\epsilon_\gamma = 0.5$ and $n = 1$. All these generation cuts can be modified via the input card, but for consistency reasons their values should be much smaller than the values used in the fiducial phase-space definition at analysis level. Note that we have explicitly checked that removing the aforementioned generation cuts does not have any impact beyond the numerical uncertainties for the observables considered in this paper. We keep them to avoid potential instabilities in the generation of events. However, in the release of the code we turn them off by default, since they might induce effects in other fiducial setups.

The Born suppression factor that we adopt is constructed in factorized form

$$B_{\text{supp}} = F_{\text{supp}}(p_{\text{T},\gamma}) \cdot G_{\text{supp}}(\Delta R_{\gamma,\ell^+}) \cdot G_{\text{supp}}(\Delta R_{\gamma,\ell^-}) \cdot H_{\text{supp}}(\Delta R_{\gamma,j}), \qquad \text{(A.1)}$$

with

$$F_{\text{supp}}(p_{\text{T},\gamma}) = \frac{(p_{\text{T},\gamma})^2}{(p_{\text{T},\gamma})^2 + (p_{\text{T},\gamma}^0)^2}, \qquad \text{with} \quad p_{\text{T},\gamma}^0 = 10\,\text{GeV}, \qquad \text{(A.2)}$$

$$G_{\text{supp}}(\Delta R) = \frac{(\Delta R)^2}{(\Delta R)^2 + (\Delta R_0)^2}, \qquad \text{with} \quad \Delta R_0 = 0.5, \qquad \text{(A.3)}$$

and

$$H_{\text{supp}}(\Delta R) = \frac{(\Delta R)^2}{(\Delta R)^2 + (\Delta R_0)^2}, \quad \text{with} \quad \Delta R_0 = 0.2. \qquad \text{(A.4)}$$

Since we apply an overall Sudakov form factor through MiNLO$'$/MiNNLO$_{\text{PS}}$, we do not need any suppression related to the outgoing parton for $Z\gamma$+jet production. It is clear that, whenever a singularity is approched, the Born suppression factor in eq. (A.1) vanishes in such a way that the cross section times Born suppression factor itself remains finite.

As discussed in section 2.3, we have a remnant contribution which is QCD regular, but QED singular. Accordingly, we introduce a remnant suppression factor of the form

$$R_{\text{supp}} = F_{\text{supp}}(p_{\text{T},\gamma}) \cdot G_{\text{supp}}(\Delta R_{\gamma,\ell^+}) \cdot G_{\text{supp}}(\Delta R_{\gamma,\ell^-}) \cdot H_{\text{supp}}(\Delta R_{\gamma,j_1})$$
$$\cdot \, H_{\text{supp}}(\Delta R_{\gamma,j_2}) \cdot H_{\text{supp}}(\Delta R_{j_1,j_2}) \cdot L_{\text{supp}}(p_{\text{T},j_2}), \qquad \text{(A.5)}$$

with

$$L_{\text{supp}}(p_{\text{T},j_2}) = \frac{(p_{\text{T},j_2})^2}{(p_{\text{T},j_2})^2 + (p_{\text{T},j_2}^0)^2}, \quad \text{with} \quad p_{\text{T},j_2}^0 = 20\,\text{GeV}. \qquad \text{(A.6)}$$

As usual in POWHEG, the Born suppression is evaluated using the Born kinematics, while the remnant suppression is evaluated using the kinematics of the real phase space. We note that in our case it is not necessary to introduce the additional factor $L_{\text{supp}}(p_{\text{T},j_2})$, however, we found that results converged more quickly with the introduction of this additional suppression factor.

B Projection from the $Z\gamma$+jet to the $Z\gamma$ phase space

The evaluation of the last term in eq. (3.15) requires a projection from the $Z\gamma$+jet to the $Z\gamma$ kinematics. In this appendix, we give details about this projection and comment on configurations, which after projection have $p_{\mathrm{T},\gamma}$ close to zero.

We denote by p_1 and p_2 the two incoming momenta, and by p_γ, p_Z and p_j the momenta of the photon, the Z boson and the jet in the final state. We define $p_{\mathrm{tot}} = p_1 + p_2 - p_j = p_\gamma + p_Z$. Our projection to the respective $Z\gamma$ configuration is the one adopted for initial-state radiation in POWHEG, which is described in section 5.5.1 of ref. [65] (cf. also appendix A of ref. [70]). It consists of a longitudinal boost (by β_{L}), such that, after boosting, p_{tot} has no z component. Then, a second boost (by $\vec{\beta}_{\mathrm{T}}$) in the transverse plane, such that p_{tot} has no transverse component, is applied, followed by a final boost back in the longitudinal direction (by $-\beta_{\mathrm{L}}$). We add a prime to all quantities after the first longitudinal boost and a double prime to those after the second one. The boost vector of the transverse boost is then given by

$$\vec{\beta}_{\mathrm{T}} = \frac{\vec{p}_{\mathrm{T},j}}{E'_{\mathrm{tot}}}\,, \tag{B.1}$$

After the second boost, the transverse momentum of the photon becomes

$$\vec{p}''_{\mathrm{T},\gamma} = \vec{p}_{\mathrm{T},\gamma}\gamma_{\mathrm{T}}\left(\vec{p}_{\mathrm{T},\gamma} + \vec{\beta}_{\mathrm{T}}E'_\gamma\right)\,, \quad \text{with} \quad \gamma_{\mathrm{T}} = \frac{1}{\sqrt{1-\beta_{\mathrm{T}}^2}}\,. \tag{B.2}$$

Therefore, after this boost, the condition $\vec{p}''_{\mathrm{T},\gamma} = 0$ is met if

$$\vec{\beta}_{\mathrm{T}} = -\frac{\vec{p}_{\mathrm{T},\gamma}}{E'_\gamma}\,. \tag{B.3}$$

By comparing eq. (B.1) and (B.3) we see that $\vec{p}_{\mathrm{T},\gamma}$ and $\vec{p}_{\mathrm{T},j}$ must be anti-aligned. Furthermore, since $E'_{\mathrm{tot}} = E'_\gamma + E'_Z > E_\gamma$ it follows that $p_{\mathrm{T},j} > p_{\mathrm{T},\gamma}$. Accordingly, any boost that leads to a vanishing transverse momentum of the photon in the $Z\gamma$ configuration has a jet that is harder than the photon in the $Z\gamma$+jet configuration. Since for the photon we impose a transverse-momentum cut, these configurations are free of any large logarithms, and the corrections from $\mathcal{D}_{\ell_{\mathrm{F}}}(p_{\mathrm{T}})$ in eqs. (3.12) and (3.13) in this region of phase space are strictly beyond our accuracy and can be dropped.

C OpenLoops vs. MCFM implementation: heavy-quark mass effects

In this appendix, we provide additional information regarding the limitation of the MiNNLO$_{\mathrm{PS}}$ generator when using MCFM amplitudes by comparing the results presented in section 4 against our alternative implementation that uses OpenLoops amplitudes. As described in detail in section 2.1, OpenLoops includes the full dependence on heavy quark masses in the one-loop amplitudes, while in the MCFM ones bottom-quark loops are included only partially and top-quark loops are omitted entirely. To assess the validity of the approximations done within the MCFM implemenation with respect to including
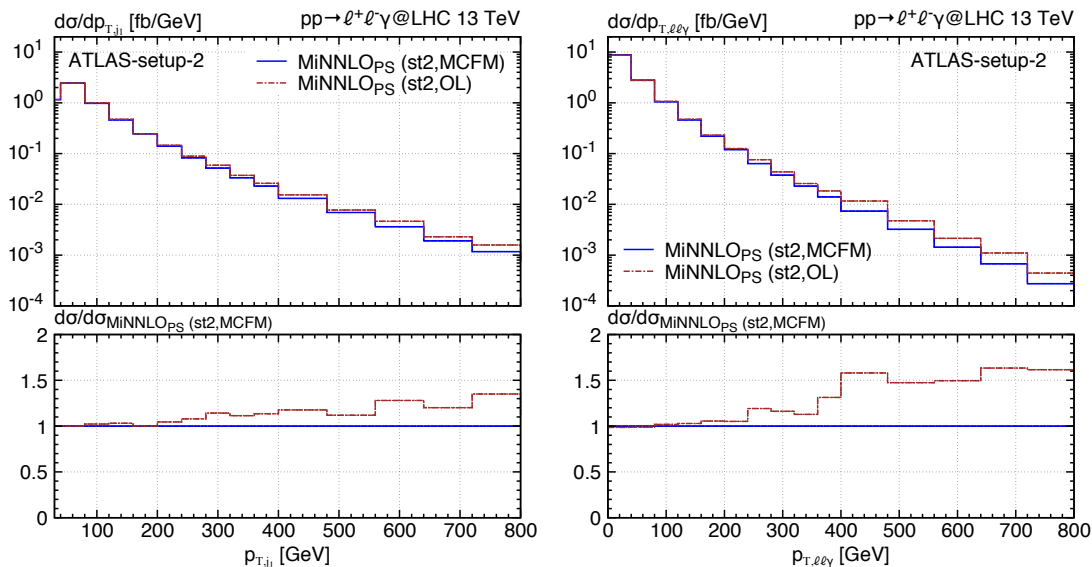
Figure 11. Comparison of MiNNLO$_\text{PS}$ predictions using MCFM (blue, solid) and using OPEN-LOOPS (brown, dash-dotted) for the distribution in the transverse momentum of the leading jet (left plot) and of the $Z\gamma$ system (right plot) at POWHEG stage 2 in `ATLAS-setup-2` (see section 4.1).

the full heavy-quark mass dependence, we consider MiNNLO$_\text{PS}$ predictions at POWHEG stage 2 using MCFM and OPENLOOPS. We have compared all distributions that we produced in `ATLAS-setup-1` and `ATLAS-setup-2` (defined in section 4.1) and found that for observables inclusive over QCD radiation heavy-quark mass effects are at the level of the numerical uncertainties and can be safely neglected. At variance, as far as observables that require hard/boosted jets are concerned, heavy-quark mass effects become important and the MCFM and OPENLOOPS results can differ substantially. For illustration and to provide relevant examples, figure 11 compares our MCFM (blue, solid) and OPENLOOPS (brown, dash-dotted) implementation of MiNNLO$_\text{PS}$ for the transverse momentum spectrum of the leading jet and of the $Z\gamma$ system in `ATLAS-setup-2` at POWHEG stage 2. Indeed, in the bulk of the cross section at low transverse momentum heavy-quark mass effects are negligible. For $p_T \gtrsim 150\,\text{GeV}$, however, we can appreciate the increase of the OPENLOOPS result with respect to MCFM, indicating the importance of heavy-quark mass effects and the limitation of the MCFM implementation.

We hope that this comparison provides useful information to any user who wants to make a choice between the two implementations.

References

[1] ATLAS collaboration, *Measurement of the $Z(\to \ell^+\ell^-)\gamma$ production cross-section in pp collisions at $\sqrt{s} = 13$ TeV with the ATLAS detector*, *JHEP* **03** (2020) 054

[arXiv:1911.04813] [INSPIRE].

[2] CMS collaboration, *Measurements of pp → ZZ production cross sections and constraints on anomalous triple gauge couplings at √s = 13 TeV*, *Eur. Phys. J. C* **81** (2021) 200 [arXiv:2009.01186] [INSPIRE].

[3] G. Ferrera, M. Grazzini and F. Tramontano, *Associated WH production at hadron colliders: a fully exclusive QCD calculation at NNLO*, *Phys. Rev. Lett.* **107** (2011) 152003 [arXiv:1107.1164] [INSPIRE].

[4] G. Ferrera, M. Grazzini and F. Tramontano, *Associated ZH production at hadron colliders: the fully differential NNLO QCD calculation*, *Phys. Lett. B* **740** (2015) 51 [arXiv:1407.4747] [INSPIRE].

[5] G. Ferrera, G. Somogyi and F. Tramontano, *Associated production of a Higgs boson decaying into bottom quarks at the LHC in full NNLO QCD*, *Phys. Lett. B* **780** (2018) 346 [arXiv:1705.10304] [INSPIRE].

[6] J.M. Campbell, R.K. Ellis and C. Williams, *Associated production of a Higgs boson at NNLO*, *JHEP* **06** (2016) 179 [arXiv:1601.00658] [INSPIRE].

[7] R.V. Harlander and W.B. Kilgore, *Higgs boson production in bottom quark fusion at next-to-next-to leading order*, *Phys. Rev. D* **68** (2003) 013001 [hep-ph/0304035] [INSPIRE].

[8] R.V. Harlander, K.J. Ozeren and M. Wiesemann, *Higgs plus jet production in bottom quark annihilation at next-to-leading order*, *Phys. Lett. B* **693** (2010) 269 [arXiv:1007.5411] [INSPIRE].

[9] R. Harlander and M. Wiesemann, *Jet-veto in bottom-quark induced Higgs production at next-to-next-to-leading order*, *JHEP* **04** (2012) 066 [arXiv:1111.2182] [INSPIRE].

[10] S. Bühler, F. Herzog, A. Lazopoulos and R. Müller, *The fully differential hadronic production of a Higgs boson via bottom quark fusion at NNLO*, *JHEP* **07** (2012) 115 [arXiv:1204.4415] [INSPIRE].

[11] S. Marzani, R.D. Ball, V. Del Duca, S. Forte and A. Vicini, *Higgs production via gluon-gluon fusion with finite top mass beyond next-to-leading order*, *Nucl. Phys. B* **800** (2008) 127 [arXiv:0801.2544] [INSPIRE].

[12] R.V. Harlander and K.J. Ozeren, *Finite top mass effects for hadronic Higgs production at next-to-next-to-leading order*, *JHEP* **11** (2009) 088 [arXiv:0909.3420] [INSPIRE].

[13] R.V. Harlander, H. Mantler, S. Marzani and K.J. Ozeren, *Higgs production in gluon fusion at next-to-next-to-leading order QCD for finite top mass*, *Eur. Phys. J. C* **66** (2010) 359 [arXiv:0912.2104] [INSPIRE].

[14] A. Pak, M. Rogal and M. Steinhauser, *Finite top quark mass effects in NNLO Higgs boson production at LHC*, *JHEP* **02** (2010) 025 [arXiv:0911.4662] [INSPIRE].

[15] T. Neumann and M. Wiesemann, *Finite top-mass effects in gluon-induced Higgs production with a jet-veto at NNLO*, *JHEP* **11** (2014) 150 [arXiv:1408.6836] [INSPIRE].

[16] D. de Florian and J. Mazzitelli, *Higgs boson pair production at next-to-next-to-leading order in QCD*, *Phys. Rev. Lett.* **111** (2013) 201801 [arXiv:1309.6594] [INSPIRE].

[17] D. de Florian et al., *Differential Higgs boson pair production at next-to-next-to-leading order in QCD*, *JHEP* **09** (2016) 151 [arXiv:1606.09519] [INSPIRE].

[18] M. Grazzini et al., *Higgs boson pair production at NNLO with top quark mass effects*, *JHEP* **05** (2018) 059 [arXiv:1803.02463] [ɪɴSPIRE].

[19] S. Catani, L. Cieri, D. de Florian, G. Ferrera and M. Grazzini, *Diphoton production at hadron colliders: a fully-differential QCD calculation at NNLO*, *Phys. Rev. Lett.* **108** (2012) 072001 [*Erratum ibid.* **117** (2016) 089901] [arXiv:1110.2375] [ɪɴSPIRE].

[20] J.M. Campbell, R.K. Ellis, Y. Li and C. Williams, *Predictions for diphoton production at the LHC through NNLO in QCD*, *JHEP* **07** (2016) 148 [arXiv:1603.02663] [ɪɴSPIRE].

[21] M. Grazzini, S. Kallweit, D. Rathlev and A. Torre, *Zγ production at hadron colliders in NNLO QCD*, *Phys. Lett. B* **731** (2014) 204 [arXiv:1309.7000] [ɪɴSPIRE].

[22] M. Grazzini, S. Kallweit and D. Rathlev, *Wγ and Zγ production at the LHC in NNLO QCD*, *JHEP* **07** (2015) 085 [arXiv:1504.01330] [ɪɴSPIRE].

[23] J.M. Campbell, T. Neumann and C. Williams, *Zγ production at NNLO including anomalous couplings*, *JHEP* **11** (2017) 150 [arXiv:1708.02925] [ɪɴSPIRE].

[24] T. Gehrmann, N. Glover, A. Huss and J. Whitehead, *Scale and isolation sensitivity of diphoton distributions at the LHC*, *JHEP* **01** (2021) 108 [arXiv:2009.11310] [ɪɴSPIRE].

[25] F. Cascioli et al., *ZZ production at hadron colliders in NNLO QCD*, *Phys. Lett. B* **735** (2014) 311 [arXiv:1405.2219] [ɪɴSPIRE].

[26] M. Grazzini, S. Kallweit and D. Rathlev, *ZZ production at the LHC: fiducial cross sections and distributions in NNLO QCD*, *Phys. Lett. B* **750** (2015) 407 [arXiv:1507.06257] [ɪɴSPIRE].

[27] G. Heinrich, S. Jahn, S.P. Jones, M. Kerner and J. Pires, *NNLO predictions for Z-boson pair production at the LHC*, *JHEP* **03** (2018) 142 [arXiv:1710.06294] [ɪɴSPIRE].

[28] S. Kallweit and M. Wiesemann, *ZZ production at the LHC: NNLO predictions for 2ℓ2ν and 4ℓ signatures*, *Phys. Lett. B* **786** (2018) 382 [arXiv:1806.05941] [ɪɴSPIRE].

[29] T. Gehrmann et al., *W⁺W⁻ production at hadron colliders in next to next to leading order QCD*, *Phys. Rev. Lett.* **113** (2014) 212001 [arXiv:1408.5243] [ɪɴSPIRE].

[30] M. Grazzini, S. Kallweit, S. Pozzorini, D. Rathlev and M. Wiesemann, *W⁺W⁻ production at the LHC: fiducial cross sections and distributions in NNLO QCD*, *JHEP* **08** (2016) 140 [arXiv:1605.02716] [ɪɴSPIRE].

[31] M. Grazzini, S. Kallweit, D. Rathlev and M. Wiesemann, *W±Z production at hadron colliders in NNLO QCD*, *Phys. Lett. B* **761** (2016) 179 [arXiv:1604.08576] [ɪɴSPIRE].

[32] M. Grazzini, S. Kallweit, D. Rathlev and M. Wiesemann, *W±Z production at the LHC: fiducial cross sections and distributions in NNLO QCD*, *JHEP* **05** (2017) 139 [arXiv:1703.09065] [ɪɴSPIRE].

[33] J. Baglio et al., *The measurement of the Higgs self-coupling at the LHC: theoretical status*, *JHEP* **04** (2013) 151 [arXiv:1212.5581] [ɪɴSPIRE].

[34] H.T. Li and J. Wang, *Fully differential Higgs pair production in association with a W boson at next-to-next-to-leading order in QCD*, *Phys. Lett. B* **765** (2017) 265 [arXiv:1607.06382] [ɪɴSPIRE].

[35] D. de Florian, I. Fabre and J. Mazzitelli, *Triple Higgs production at hadron colliders at NNLO in QCD*, *JHEP* **03** (2020) 155 [arXiv:1912.02760] [ɪɴSPIRE].

[36] H.A. Chawdhry, M.L. Czakon, A. Mitov and R. Poncelet, *NNLO QCD corrections to three-photon production at the LHC*, *JHEP* **02** (2020) 057 [arXiv:1911.00479] [INSPIRE].

[37] S. Kallweit, V. Sotnikov and M. Wiesemann, *Triphoton production at hadron colliders in NNLO QCD*, *Phys. Lett. B* **812** (2021) 136013 [arXiv:2010.04681] [INSPIRE].

[38] CMS collaboration, *Measurement of $W\gamma$ and $Z\gamma$ production in pp collisions at $\sqrt{s} = 7$ TeV*, *Phys. Lett. B* **701** (2011) 535 [arXiv:1105.2758] [INSPIRE].

[39] ATLAS collaboration, *Measurement of Wgamma and Zgamma production in proton-proton collisions at $\sqrt{s} = 7$ TeV with the ATLAS Detector*, *JHEP* **09** (2011) 072 [arXiv:1106.1592] [INSPIRE].

[40] ATLAS collaboration, *Measurement of $W\gamma$ and $Z\gamma$ production cross sections in pp collisions at $\sqrt{s} = 7$ TeV and limits on anomalous triple gauge couplings with the ATLAS detector*, *Phys. Lett. B* **717** (2012) 49 [arXiv:1205.2531] [INSPIRE].

[41] CMS collaboration, *Measurement of the $W\gamma$ and $Z\gamma$ inclusive cross sections in pp collisions at $\sqrt{s} = 7$ TeV and limits on anomalous triple gauge boson couplings*, *Phys. Rev. D* **89** (2014) 092005 [arXiv:1308.6832] [INSPIRE].

[42] CMS collaboration, *Measurement of the production cross section for $Z\gamma \to \nu\bar{\nu}\gamma$ in pp collisions at $\sqrt{s} = 7$ TeV and limits on $ZZ\gamma$ and $Z\gamma\gamma$ triple gauge boson couplings*, *JHEP* **10** (2013) 164 [arXiv:1309.1117] [INSPIRE].

[43] ATLAS collaboration, *Measurements of $W\gamma$ and $Z\gamma$ production in pp collisions at $\sqrt{s} = 7$ TeV with the ATLAS detector at the LHC*, *Phys. Rev. D* **87** (2013) 112003 [*Erratum ibid.* **91** (2015) 119901] [arXiv:1302.1283] [INSPIRE].

[44] ATLAS collaboration, *Search for new resonances in $W\gamma$ and $Z\gamma$ final states in pp collisions at $\sqrt{s} = 8$ TeV with the ATLAS detector*, *Phys. Lett. B* **738** (2014) 428 [arXiv:1407.8150] [INSPIRE].

[45] CMS collaboration, *Measurement of the $Z\gamma$ production cross section in pp collisions at 8 TeV and search for anomalous triple gauge boson couplings*, *JHEP* **04** (2015) 164 [arXiv:1502.05664] [INSPIRE].

[46] CMS collaboration, *Measurement of the $Z\gamma \to \nu\bar{\nu}\gamma$ production cross section in pp collisions at $\sqrt{s} = 8$ TeV and limits on anomalous $ZZ\gamma$ and $Z\gamma\gamma$ trilinear gauge boson couplings*, *Phys. Lett. B* **760** (2016) 448 [arXiv:1602.07152] [INSPIRE].

[47] ATLAS collaboration, *Measurements of $Z\gamma$ and $Z\gamma\gamma$ production in pp collisions at $\sqrt{s} = 8$ TeV with the ATLAS detector*, *Phys. Rev. D* **93** (2016) 112002 [arXiv:1604.05232] [INSPIRE].

[48] ATLAS collaboration, *Measurement of the $Z\gamma \to \nu\bar{\nu}\gamma$ production cross section in pp collisions at $\sqrt{s} = 13$ TeV with the ATLAS detector and limits on anomalous triple gauge-boson couplings*, *JHEP* **12** (2018) 010 [arXiv:1810.04995] [INSPIRE].

[49] CMS collaboration, *Search for the decay of a Higgs boson in the $\ell\ell\gamma$ channel in proton-proton collisions at $\sqrt{s} = 13$ TeV*, *JHEP* **11** (2018) 152 [arXiv:1806.05996] [INSPIRE].

[50] ATLAS collaboration, *A search for the $Z\gamma$ decay mode of the Higgs boson in pp collisions at $\sqrt{s} = 13$ TeV with the ATLAS detector*, *Phys. Lett. B* **809** (2020) 135754 [arXiv:2005.05382] [INSPIRE].

[51] J. Ohnemus, *Order α^-s calculations of hadronic $W^{\pm}\gamma$ and $Z\gamma$ production*, *Phys. Rev. D* **47** (1993) 940 [INSPIRE].

[52] U. Baur, T. Han and J. Ohnemus, *QCD corrections and anomalous couplings in $Z\gamma$ production at hadron colliders*, *Phys. Rev. D* **57** (1998) 2823 [hep-ph/9710416] [INSPIRE].

[53] L. Ametller, E. Gava, N. Paver and D. Treleani, *Role of the QCD induced gluon-gluon coupling to gauge boson pairs in the multi-TeV region*, *Phys. Rev. D* **32** (1985) 1699 [INSPIRE].

[54] J.J. van der Bij and E.W.N. Glover, *Photon Z boson pair production via gluon fusion*, *Phys. Lett. B* **206** (1988) 701 [INSPIRE].

[55] K.L. Adamson, D. de Florian and A. Signer, *Gluon induced contributions to $Z\gamma$ production at hadron colliders*, *Phys. Rev. D* **67** (2003) 034016 [hep-ph/0211295] [INSPIRE].

[56] J.M. Campbell, R.K. Ellis and C. Williams, *Vector boson pair production at the LHC*, *JHEP* **07** (2011) 018 [arXiv:1105.0020] [INSPIRE].

[57] W. Hollik and C. Meier, *Electroweak corrections to γZ production at hadron colliders*, *Phys. Lett. B* **590** (2004) 69 [hep-ph/0402281] [INSPIRE].

[58] E. Accomando, A. Denner and C. Meier, *Electroweak corrections to $W\gamma$ and $Z\gamma$ production at the LHC*, *Eur. Phys. J. C* **47** (2006) 125 [hep-ph/0509234] [INSPIRE].

[59] M. Wiesemann, L. Rottoli and P. Torrielli, *The $Z\gamma$ transverse-momentum spectrum at $NNLO+N^3LL$*, *Phys. Lett. B* **809** (2020) 135718 [arXiv:2006.09338] [INSPIRE].

[60] T. Becher and T. Neumann, *Fiducial q_T resummation of color-singlet processes at $N^3LL+NNLO$*, *JHEP* **03** (2021) 199 [arXiv:2009.11437] [INSPIRE].

[61] S. Kallweit, E. Re, L. Rottoli and M. Wiesemann, *Accurate single- and double-differential resummation of colour-singlet processes with MATRIX+RADISH: W^+W^- production at the LHC*, *JHEP* **12** (2020) 147 [arXiv:2004.07720] [INSPIRE].

[62] M. Dasgupta, F.A. Dreyer, K. Hamilton, P.F. Monni, G.P. Salam and G. Soyez, *Parton showers beyond leading logarithmic accuracy*, *Phys. Rev. Lett.* **125** (2020) 052002 [arXiv:2002.11114] [INSPIRE].

[63] S. Frixione and B.R. Webber, *Matching NLO QCD computations and parton shower simulations*, *JHEP* **06** (2002) 029 [hep-ph/0204244] [INSPIRE].

[64] P. Nason, *A new method for combining NLO QCD with shower Monte Carlo algorithms*, *JHEP* **11** (2004) 040 [hep-ph/0409146] [INSPIRE].

[65] S. Frixione, P. Nason and C. Oleari, *Matching NLO QCD computations with Parton Shower simulations: the POWHEG method*, *JHEP* **11** (2007) 070 [arXiv:0709.2092] [INSPIRE].

[66] J. Krause and F. Siegert, *NLO QCD predictions for $Z + \gamma$ + jets production with Sherpa*, *Eur. Phys. J. C* **78** (2018) 161 [arXiv:1708.06283] [INSPIRE].

[67] K. Hamilton, P. Nason, C. Oleari and G. Zanderighi, *Merging $H/W/Z + 0$ and 1 jet at NLO with no merging scale: a path to parton shower + NNLO matching*, *JHEP* **05** (2013) 082 [arXiv:1212.4504] [INSPIRE].

[68] S. Alioli, C.W. Bauer, C. Berggren, F.J. Tackmann, J.R. Walsh and S. Zuberi, *Matching fully differential NNLO calculations and parton showers*, *JHEP* **06** (2014) 089 [arXiv:1311.0286] [INSPIRE].

[69] S. Höche, Y. Li and S. Prestel, *Drell-Yan lepton pair production at NNLO QCD with parton showers*, *Phys. Rev. D* **91** (2015) 074015 [arXiv:1405.3607] [ɪɴSPIRE].

[70] P.F. Monni, P. Nason, E. Re, M. Wiesemann and G. Zanderighi, *MiNNLO$_{PS}$: a new method to match NNLO QCD to parton showers*, *JHEP* **05** (2020) 143 [arXiv:1908.06987] [ɪɴSPIRE].

[71] P.F. Monni, E. Re and M. Wiesemann, *MiNNLO$_{PS}$: optimizing $2 \to 1$ hadronic processes*, *Eur. Phys. J. C* **80** (2020) 1075 [arXiv:2006.04133] [ɪɴSPIRE].

[72] K. Hamilton, P. Nason and G. Zanderighi, *MINLO: Multi-scale Improved NLO*, *JHEP* **10** (2012) 155 [arXiv:1206.3572] [ɪɴSPIRE].

[73] R. Frederix and K. Hamilton, *Extending the MINLO method*, *JHEP* **05** (2016) 042 [arXiv:1512.02663] [ɪɴSPIRE].

[74] K. Hamilton, P. Nason, E. Re and G. Zanderighi, *NNLOPS simulation of Higgs boson production*, *JHEP* **10** (2013) 222 [arXiv:1309.0017] [ɪɴSPIRE].

[75] S. Höche, Y. Li and S. Prestel, *Higgs-boson production through gluon fusion at NNLO QCD with parton showers*, *Phys. Rev. D* **90** (2014) 054011 [arXiv:1407.3773] [ɪɴSPIRE].

[76] A. Karlberg, E. Re and G. Zanderighi, *NNLOPS accurate Drell-Yan production*, *JHEP* **09** (2014) 134 [arXiv:1407.2940] [ɪɴSPIRE].

[77] S. Alioli, C.W. Bauer, C. Berggren, F.J. Tackmann and J.R. Walsh, *Drell-Yan production at NNLL'+NNLO matched to parton showers*, *Phys. Rev. D* **92** (2015) 094020 [arXiv:1508.01475] [ɪɴSPIRE].

[78] W. Astill, W. Bizon, E. Re and G. Zanderighi, *NNLOPS accurate associated HW production*, *JHEP* **06** (2016) 154 [arXiv:1603.01620] [ɪɴSPIRE].

[79] W. Astill, W. Bizoń, E. Re and G. Zanderighi, *NNLOPS accurate associated HZ production with $H \to b\bar{b}$ decay at NLO*, *JHEP* **11** (2018) 157 [arXiv:1804.08141] [ɪɴSPIRE].

[80] S. Alioli, A. Broggio, S. Kallweit, M.A. Lim and L. Rottoli, *Higgsstrahlung at NNLL'+NNLO matched to parton showers in GENEVA*, *Phys. Rev. D* **100** (2019) 096016 [arXiv:1909.02026] [ɪɴSPIRE].

[81] W. Bizoń, E. Re and G. Zanderighi, *NNLOPS description of the $H \to b\bar{b}$ decay with MiNLO*, *JHEP* **06** (2020) 006 [arXiv:1912.09982] [ɪɴSPIRE].

[82] S. Alioli et al., *Resummed predictions for hadronic Higgs boson decays*, *JHEP* **04** (2021) 254 [arXiv:2009.13533] [ɪɴSPIRE].

[83] E. Re, M. Wiesemann and G. Zanderighi, *NNLOPS accurate predictions for W^+W^- production*, *JHEP* **12** (2018) 121 [arXiv:1805.09857] [ɪɴSPIRE].

[84] K. Hamilton, T. Melia, P.F. Monni, E. Re and G. Zanderighi, *Merging WW and WW + jet with MINLO*, *JHEP* **09** (2016) 057 [arXiv:1606.07062] [ɪɴSPIRE].

[85] M. Grazzini, S. Kallweit and M. Wiesemann, *Fully differential NNLO computations with MATRIX*, *Eur. Phys. J. C* **78** (2018) 537 [arXiv:1711.06631] [ɪɴSPIRE].

[86] J.C. Collins and D.E. Soper, *Angular distribution of dileptons in high-energy hadron collisions*, *Phys. Rev. D* **16** (1977) 2219 [ɪɴSPIRE].

[87] S. Alioli, P. Nason, C. Oleari and E. Re, *A general framework for implementing NLO calculations in shower Monte Carlo programs: the POWHEG BOX*, *JHEP* **06** (2010) 043 [arXiv:1002.2581] [ɪɴSPIRE].

[88] T. Ježo and P. Nason, *On the treatment of resonances in next-to-leading order calculations matched to a parton shower*, *JHEP* **12** (2015) 065 [arXiv:1509.09071] [INSPIRE].

[89] J. Campbell and T. Neumann, *Precision phenomenology with MCFM*, *JHEP* **12** (2019) 034 [arXiv:1909.09117] [INSPIRE].

[90] F. Cascioli, P. Maierhofer and S. Pozzorini, *Scattering amplitudes with open loops*, *Phys. Rev. Lett.* **108** (2012) 111601 [arXiv:1111.5206] [INSPIRE].

[91] F. Buccioni, S. Pozzorini and M. Zoller, *On-the-fly reduction of open loops*, *Eur. Phys. J. C* **78** (2018) 70 [arXiv:1710.11452] [INSPIRE].

[92] F. Buccioni et al., *OpenLoops 2*, *Eur. Phys. J. C* **79** (2019) 866 [arXiv:1907.13071] [INSPIRE].

[93] L.J. Dixon, Z. Kunszt and A. Signer, *Helicity amplitudes for $O(\alpha_s)$ production of W^+W^-, $W^\pm Z$, ZZ, $W^\pm\gamma$, or $Z\gamma$ pairs at hadron colliders*, *Nucl. Phys. B* **531** (1998) 3 [hep-ph/9803250] [INSPIRE].

[94] D. De Florian and A. Signer, *$W\gamma$ and $Z\gamma$ production at hadron colliders*, *Eur. Phys. J. C* **16** (2000) 105 [hep-ph/0002138] [INSPIRE].

[95] J.M. Campbell, H.B. Hartanto and C. Williams, *Next-to-leading order predictions for $Z\gamma$+jet and $Z\gamma\gamma$ final states at the LHC*, *JHEP* **11** (2012) 162 [arXiv:1208.0566] [INSPIRE].

[96] J.M. Campbell and R.K. Ellis, *Top-quark loop corrections in Z + jet and Z + 2 jet production*, *JHEP* **01** (2017) 020 [arXiv:1610.02189] [INSPIRE].

[97] S. Alioli, P. Nason, C. Oleari and E. Re, *Vector boson plus one jet production in POWHEG*, *JHEP* **01** (2011) 095 [arXiv:1009.5594] [INSPIRE].

[98] T. Jezo, M. Klasen and F. König, *Prompt photon production and photon-hadron jet correlations with POWHEG*, *JHEP* **11** (2016) 033 [arXiv:1610.02275] [INSPIRE].

[99] S. Frixione, *Isolated photons in perturbative QCD*, *Phys. Lett. B* **429** (1998) 369 [hep-ph/9801442] [INSPIRE].

[100] S. Catani, L. Cieri, D. de Florian, G. Ferrera and M. Grazzini, *Diphoton production at the LHC: a QCD study up to NNLO*, *JHEP* **04** (2018) 142 [arXiv:1802.02095] [INSPIRE].

[101] L. Barze et al., *$W\gamma$ production in hadronic collisions using the POWHEG+MiNLO method*, *JHEP* **12** (2014) 039 [arXiv:1408.5766] [INSPIRE].

[102] M. Klasen, C. Klein-Bösing and H. Poppenborg, *Prompt photon production and photon-jet correlations at the LHC*, *JHEP* **03** (2018) 081 [arXiv:1709.04154] [INSPIRE].

[103] S. Alioli, P. Nason, C. Oleari and E. Re, *NLO vector-boson production matched with shower in POWHEG*, *JHEP* **07** (2008) 060 [arXiv:0805.4802] [INSPIRE].

[104] V. Hirschi and O. Mattelaer, *Automated event generation for loop-induced processes*, *JHEP* **10** (2015) 146 [arXiv:1507.00020] [INSPIRE].

[105] T. Gehrmann and L. Tancredi, *Two-loop QCD helicity amplitudes for $q\bar{q} \to W^\pm\gamma$ and $q\bar{q} \to Z^0\gamma$*, *JHEP* **02** (2012) 004 [arXiv:1112.1531] [INSPIRE].

[106] M. Grazzini, S. Kallweit and M. Wiesemann, *Matrix — Munich Automates qT subtraction and Resummation to Integrate X-sections*, http://matrix.hepforge.org.

[107] M. Grazzini, S. Kallweit, D. Rathlev and M. Wiesemann, *Transverse-momentum resummation for vector-boson pair production at NNLL+NNLO*, *JHEP* **08** (2015) 154 [arXiv:1507.02565] [INSPIRE].

[108] P.F. Monni, E. Re and P. Torrielli, *Higgs transverse-momentum resummation in direct space*, *Phys. Rev. Lett.* **116** (2016) 242001 [arXiv:1604.02191] [INSPIRE].

[109] W. Bizon, P.F. Monni, E. Re, L. Rottoli and P. Torrielli, *Momentum-space resummation for transverse observables and the Higgs $p_\perp$ at $N^3LL+NNLO$*, *JHEP* **02** (2018) 108 [arXiv:1705.09127] [INSPIRE].

[110] P.F. Monni, L. Rottoli and P. Torrielli, *Higgs transverse momentum with a jet veto: a double-differential resummation*, *Phys. Rev. Lett.* **124** (2020) 252001 [arXiv:1909.04704] [INSPIRE].

[111] S. Catani and M. Grazzini, *QCD transverse-momentum resummation in gluon fusion processes*, *Nucl. Phys. B* **845** (2011) 297 [arXiv:1011.3918] [INSPIRE].

[112] S. Catani, L. Cieri, D. de Florian, G. Ferrera and M. Grazzini, *Universality of transverse-momentum resummation and hard factors at the NNLO*, *Nucl. Phys. B* **881** (2014) 414 [arXiv:1311.1654] [INSPIRE].

[113] S. Catani, D. de Florian and M. Grazzini, *Universality of nonleading logarithmic contributions in transverse momentum distributions*, *Nucl. Phys. B* **596** (2001) 299 [hep-ph/0008184] [INSPIRE].

[114] P. Nason and C. Oleari, *Generation cuts and Born suppression in POWHEG*, arXiv:1303.3922 [INSPIRE].

[115] T. Sjöstrand et al., *An introduction to PYTHIA 8.2*, *Comput. Phys. Commun.* **191** (2015) 159 [arXiv:1410.3012] [INSPIRE].

[116] B. Cabouat and T. Sjöstrand, *Some dipole shower studies*, *Eur. Phys. J. C* **78** (2018) 226 [arXiv:1710.00391] [INSPIRE].

[117] NNPDF collaboration, *Parton distributions for the LHC run II*, *JHEP* **04** (2015) 040 [arXiv:1410.8849] [INSPIRE].

[118] A. Buckley et al., *LHAPDF6: parton density access in the LHC precision era*, *Eur. Phys. J. C* **75** (2015) 132 [arXiv:1412.7420] [INSPIRE].

[119] G.P. Salam and J. Rojo, *A Higher Order Perturbative Parton Evolution Toolkit (HOPPET)*, *Comput. Phys. Commun.* **180** (2009) 120 [arXiv:0804.3755] [INSPIRE].

[120] T. Gehrmann and E. Remiddi, *Numerical evaluation of harmonic polylogarithms*, *Comput. Phys. Commun.* **141** (2001) 296 [hep-ph/0107173] [INSPIRE].

[121] ATLAS collaboration, *ATLAS PYTHIA 8 tunes to 7 TeV data*, ATL-PHYS-PUB-2014-021 (2014).

[122] S. Catani and B.R. Webber, *Infrared safe but infinite: soft gluon divergences inside the physical region*, *JHEP* **10** (1997) 005 [hep-ph/9710333] [INSPIRE].

[123] S. Alioli et al., *Precise predictions for photon pair production matched to parton showers in GENEVA*, *JHEP* **04** (2021) 041 [arXiv:2010.10498] [INSPIRE].